Joint analysis of gravitational lensing, clustering, and abundance: Toward the unification of large-scale structure analysis

Yoo, Jaiyul ; Seljak, Uroš

DOI: https://doi.org/10.1103/PhysRevD.86.083504

Joint Analysis of Gravitational Lensing, Clustering and Abundance: Toward the Unification of Large-Scale Structure Analysis

Jaiyul Yoo[1,2*] and Uroš Seljak[1,2,3,4]
[1]*Institute for Theoretical Physics, University of Zürich, CH-8057 Zürich, Switzerland*
[2]*Lawrence Berkeley National Laboratory, University of California, Berkeley, CA 94720, USA*
[3]*Physics Department and Astronomy Department, University of California, Berkeley, CA 94720, USA and*
[4]*Institute for the Early Universe, Ewha Womans University, 120-750 Seoul, South Korea*

We explore three different methods based on weak lensing to extract cosmological constraints from the large-scale structure. In the first approach (method I: Seljak *et. al.* 2005), small-scale galaxy or cluster lensing measurements of their halo mass provide a constraint on the halo bias, which can be combined with the large-scale galaxy or cluster clustering to measure the dark matter clustering. In the second approach (method II: Baldauf *et. al.* 2010), large-scale galaxy clustering and large-scale galaxy-galaxy lensing each trace the large-scale dark matter clustering, and the two can be combined into a direct measurement of the dark matter clustering. These two methods can be combined into one method I+II to make use of lensing measurements on all scales. In the third approach (method III), we add abundance information to the method I, which is a version of self-calibrated cluster abundance method. We explore the statistical power of these three approaches as a function of galaxy or cluster luminosity to investigate the optimal mass range for each method and their cosmological constraining power. In the case of the SDSS, we find that the three methods give comparable constraints, but not in the same mass range: the method II works best for halos of $M \sim 10^{13} M_\odot$, typical of luminous red galaxies, and the methods I and III work best for halos of $M \sim 10^{14} M_\odot$, typical of low mass clusters. We discuss the robustness of each method against various systematics. Furthermore, we extend the analysis to the future large-scale galaxy surveys and find that the cluster abundance method is *not* superior to the combined method I+II, both in terms of statistical power and robustness against systematic errors. The cosmic shear-shear correlation analysis in the future surveys yields constraints as strong as the combined method, but suffer from additional systematic effects. We thus advocate the combined analysis of clustering and lensing (method I+II) as a powerful alternative to other large-scale probes. Our analysis provides a guidance to observers planning large-scale galaxy surveys such as the DES, Euclid, and the LSST.

PACS numbers: 98.80.-k,98.65.-r,98.80.Jk,98.62.Py

I. INTRODUCTION

Large-area galaxy surveys like the Sloan Digital Sky Survey (SDSS; [1, 2]) have enabled high-precision measurements of galaxy clustering over a wide range of separation, and galaxy clustering has now become a commonly exercised and indispensable tool in cosmology. While galaxies are generally expected to trace the dark matter distribution up to an overall factor on large scales [3], its relation becomes complicated on small scales, and inferring cosmological parameters from galaxy clustering measurements are, therefore, hampered by the complex relation between the galaxy and the dark matter distributions, known as galaxy bias b_g. In the linear regime, measurements of the galaxy power spectrum in redshift space [4] provide ways to break the degeneracy by constraining the parameter combination f/b_g, where f is the logarithmic growth rate. However, the recent analysis of the SDSS redshift-space distortion yields a relatively large uncertainties $\sim 30\%$ in the linear regime [5], and its full potential remains to be realized in future surveys with larger sky coverage (see, e.g., [6–10] for other approaches to modeling redshift-space distortions on small scales).

Gravitational lensing uses the subtle distortion of background source galaxy shapes to statistically map the foreground matter distribution that causes the gravitational shear (e.g., [11–13]). Especially, galaxy-galaxy lensing measures the distortion in background source galaxy shapes around the foreground lensing galaxies [14–18]. With the statistical power present in the SDSS, high precision $(20 - 30\sigma)$ measurements of galaxy-galaxy lensing signals are typically available for various galaxy samples, making it a useful tool for cosmology (see, e.g., [18–20]). Furthermore, spectroscopic redshift measurements of the foreground lens galaxies allow the galaxy-galaxy lensing signals γ to be related to the excess surface density $\Delta\Sigma$ at the lens redshift [21], which in turn is related to the galaxy-matter cross-correlation ξ_{gm}.

The combination of galaxy-galaxy lensing and galaxy clustering measurements is, therefore, helpful in breaking the degeneracy in galaxy bias b_g and measuring the matter fluctuation amplitude σ_8 (see, e.g., [22–29]). In this work we perform a systematic investigation of the cosmological constraining power that can be derived in the current and future galaxy surveys by combining both measurements of galaxy clustering and galaxy-galaxy lensing. In particular, we are interested in gaining the physical insights of the resulting constraints in a model independent way.

In response to the recent development in numerical simulations and large-scale galaxy surveys, a halo model based approach to modeling galaxy clustering and galaxy-galaxy lensing has been developed [22, 32–36]. The key part of these approaches is to assume the halo occupation distribution (HOD) and the spatial distribution of satellite galaxies, and to relate

*jyoo@physik.uzh.ch

TABLE I: SDSS galaxy samples. The approximate numbers for the SDSS galaxy samples are taken [30, 31] to represent the SDSS Main, LRG, and maxBCG samples. The mean mass $\bar{M}$ of the galaxy samples is obtained from the galaxy-galaxy lensing measurements [18, 31]. The minimum mass $M_{\rm min}$ and the maximum mass $M_{\rm max}$ are obtained by matching the number density and the mean mass of each sample. All masses are in units of $h^{-1}M_\odot$.

sample	$M_r^{0.1}+5\log h$	$N_{\rm tot}$	$n_g\ (h^{-1}{\rm Mpc})^3$	$\bar{M}$	$M_{\rm min}$	$M_{\rm max}$	$\bar{z}$
L1	-18 to -17	5900	2.0×10^{-2}	8.8×10^{10}	6.1×10^{10}	1.3×10^{11}	0.03
L2	-19 to -18	18,000	1.3×10^{-2}	3.4×10^{11}	1.7×10^{11}	8.2×10^{11}	0.04
L3	-20 to -19	44,000	1.0×10^{-2}	4.3×10^{11}	2.2×10^{11}	9.5×10^{11}	0.06
L4	-21 to -20	100,000	5.3×10^{-3}	1.2×10^{12}	5.2×10^{11}	3.6×10^{12}	0.10
L5	-22 to -21	69,000	1.0×10^{-3}	5.4×10^{12}	2.9×10^{12}	1.2×10^{13}	0.15
LRG	-23.6 to -21.6	62,000	1.0×10^{-4}	3.8×10^{13}	2.3×10^{13}	7.4×10^{13}	0.28
BCG1	-24.0 to -22.5	8500	3.0×10^{-5}	1.0×10^{14}	6.1×10^{13}	2.1×10^{14}	0.25
BCG2	-24.0 to -22.5	850	3.0×10^{-6}	3.0×10^{14}	2.1×10^{14}	5.8×10^{14}	0.25
BCG3	-24.0 to -22.5	85	3.0×10^{-7}	6.0×10^{14}	4.7×10^{14}	2.8×10^{15}	0.25

the dark matter distribution to the galaxy distributions (see, e.g., [37]). However, many parameters and assumptions of the models make it somewhat difficult to untangle the true cosmological constraining power. In particular, small-scale galaxy clustering information (roughly defined to be below twice the virial radius of the largest halos) is used for inferring HOD parameters of the model such as the satellite fraction and their radial distribution inside halos. While this information provides useful constraints on HOD parameters, it is difficult to derive any useful cosmological information with it. Moreover, the limited number of HOD parameters explored to date may artificially provide tighter constraints on the cosmological parameters. To avoid this concern we take a simpler approach to the problem by approximating galaxy samples as individual halos with a certain range of mass. This approach is equivalent to identifying central galaxies and to removing satellites in the galaxy samples. Therefore, there is no useful galaxy clustering signal on small scales.

Without the complication of the spatial galaxy distribution and the halo occupation distribution, we can compute the galaxy clustering and gravitational lensing signals in a robust and model-independent way. Galaxy clustering arises from the halo clustering and is tracing a biased version of the dark matter clustering on large scales, while galaxy-galaxy lensing can be split into two regimes. Small-scale galaxy-galaxy lensing measures the density profiles of dark matter halos and estimates its mass, and large-scale galaxy-galaxy lensing measures the cross-correlation of the dark matter and the halo distributions. We analyze three different methods to extract cosmological information. In the method I, we use small-scale lensing around galaxies to determine the halo mass, which in turn determines their large-scale bias using theoretical mass-bias relation. Once the bias is known one can use galaxy autocorrelation to determine the dark matter clustering. This approach was first attempted in [38] using the Main sample of the SDSS galaxies with limited success. We will show here that higher mass samples offer a better chance of success. The method II combines large-scale lensing and clustering to eliminate bias, and has been developed in detail in [27]. The method III adds abundance information to the method I, and becomes a specific implementation of the cluster abundance method [39, 40]. Traditional cluster abundance methods rank clusters by their mass and determine their abundance as a function of it. Two main issues in cluster abundance methods are getting correct mass of the clusters and determining the scatter between the mass observable and the mass, since both mass calibration and scatter are completely degenerate with cosmological parameters [41]. One can determine mass calibration with small-scale lensing and scatter with large-scale clustering analysis, hence the method III uses the same information as the method I with added cluster abundance information.

In this paper, we investigate the cosmological constraining power of combining galaxy clustering and galaxy-galaxy lensing and focus on finding galaxy samples that are best suited for this purpose in the SDSS. Furthermore, we attempt to answer the same questions in future galaxy surveys by extending our analysis to higher redshift. Since numerous ongoing and planned future surveys are equipped with deep and wide imaging capability, there exists another and potentially more powerful way to avoid the complication of galaxy bias and to directly map the matter distribution: Using the cosmic shear-shear power spectrum [42–44]. Measurements of the auto-correlation of subtle shape distortions, however, have proved to be difficult due to the intrinsically weak signal-to-noise ratio and numerous systematic uncertainties [45–49]. Since the first detections [50–53], only a handful of new measurements have appeared, mostly using narrow but deeply imaged areas, such as from the Hubble Space Telescope [54, 55], and the Canada-France-Hawaii Telescope [56]. Repeat imaging of the narrow stripe-82 in the SDSS enables measurements of cosmic shear of about 200 square degrees [57–59], and no larger-scale weak lensing surveys exist yet. We consider the cosmic shear measurements as another component of gravitational lensing in future galaxy surveys and compare the resulting constraints to the combined constraints of galaxy clustering and galaxy-galaxy lensing. In our analysis we do not include redshift-space distortions, which is another way to extract the information about the galaxy bias. Redshift-space disortions suffer from significant nonlinear and scale-dependent bias is-

sues [60] and need to be understood better before they can be used for high precision cosmology.

The organization of the paper is as follows. In Sec. II we present our model for the SDSS galaxy samples and discuss their physical properties. In Sec. III we present three model-independent ways to combine measurements of gravitational lensing and galaxy clustering: Small-scale galaxy-galaxy lensing and large-scale galaxy clustering in Sec. III B, large-scale galaxy-galaxy lensing and large-scale galaxy clustering in Sec. III C, and additional abundance information in Sec. III D. Large-scale galaxy clustering is briefly discussed in Sec. III A, and the combination of various methods is presented in Sec. III E. In Sec. IV, we extend our analysis to the future galaxy surveys such as the DES, BigBOSS, Euclid, and the LSST. The cosmic shear constraints are complemented and compared to the galaxy-galaxy lensing and galaxy clustering constraints in the future surveys. We summarize our results and discuss the implications for planning large-scale galaxy surveys in Sec. V. Our calculations are performed by assuming a flat ΛCDM universe with the matter density $\Omega_m = 0.23$, the matter fluctuation amplitude $\sigma_8 = 0.81$, and the spectral index $n_s = 0.97$. The matter power spectrum shape is kept fixed in cosmological parameter variations.

II. SDSS GALAXY SAMPLES

Here we describe our simple model for the SDSS galaxy samples, which will be used to investigate their cosmological constraining power. The SDSS [1, 2] completed its observation in 2008 and mapped the sky over 8000 deg^2 in five photometric bands to a limiting magnitude r =22.5. We consider nine galaxy samples that closely match the observed SDSS galaxy luminosity-bin samples: The SDSS Main galaxy (L1∼L6), the luminous red galaxy (LRG), and the maxBCG samples (e.g., [2, 30, 61–65]). However, as the SDSS Main L6 sample largely overlaps with the LRG sample, we consider only the first five galaxy samples among the SDSS Main samples. Furthermore, while there exist faint and bright LRG subsamples [61, 62], we combine both LRG samples into a single LRG sample. Finally, the maxBCG samples representing the most massive clusters are considered with three subsamples, each of which differs in richness threshold and hence in mass. Our hypothetical galaxy samples are constructed to represent the observed SDSS galaxy samples and cover a wide range of mass. The details of the SDSS galaxy samples are described in Table I.

We approximate these SDSS luminosity-bin samples as isolated central galaxies occupying individual dark matter halos. This approximation is valid for bright galaxy samples, as the satellite fraction in typical LRGs is shown to be around $3-5\%$ [19, 66], while the approximation breaks down for faint galaxy samples, where a sizable fraction are satellite galaxies that belong to a group or a cluster of galaxies. However, instead of modeling those galaxy samples with more free parameters and assumptions, we rely on various methods that remove satellite galaxies and identify central galaxies (e.g., see [67]). In this way, we can eliminate the uncertainties associated with nonlinear modeling of galaxies on small scales and focus on the cosmological constraining power that each galaxy sample represents.

Figure 1 describes our model for the SDSS galaxy samples. The top panel shows the relation between the halo masses and the central galaxy luminosity. The luminosity of the SDSS galaxy samples are obtained by using the K-corrected rest-frame r-band magnitude [68], and their mass ranges $(M_{\rm min}, M_{\rm max})$ shown as gray boxes are obtained by matching the observed number density n_g and the mean mass $\bar{M}$ (thick vertical lines) from the galaxy-galaxy lensing measurements [18, 31]. The dashed curve shows the best-fit relation for the halo mass and the central galaxy luminosity [30], obtained by analyzing the observed SDSS galaxy clustering within the luminosity range shown as the dotted lines. We extrapolate the relation (solid) beyond its validity regime to represent the LRG and the maxBCG samples, but we modify the relation to account for the fact that the central galaxies at these clusters are just as bright as the LRGs, while the combined luminosity of clusters is higher.

The four bottom panels in Figure 1 show the number density n_g, the total number $N_{\rm tot}$, the average volume $V_{\rm avg}$, and the mean redshift $\bar{z}$ for the SDSS galaxy samples with their mean mass and mass range shown as points and horizontal bars, respectively. The number density and the total number of galaxies are measured quantities, from which we infer the average volume and the mean redshift for each sample.

Furthermore, we extend our approximation for the galaxy samples to all mass range and construct continuous mass-bin samples. The continuous mass-bin samples are composed of halos with the mass-bin interval $\Delta \ln M = 1.0$ at each mass. Figure 1a plots the the number density (solid) of the continuous mass-bin samples with their mass range (dotted) as a function of the mean mass. The mass-bin interval is chosen to match the observed SDSS galaxy samples (points). The other physical quantities $N_{\rm tot}$, $V_{\rm avg}$, and $\bar{z}$ are shown as the solid curves in the other panels.

Low mass faint galaxies are abundant but probe small volume, while the massive luminous galaxies are rare but measured at larger distance. Therefore, the total number of galaxies are bounded at very low and high masses. The continuous mass-bin samples are good approximations to the observed SDSS galaxy samples, with one exception for the LRG sample, since the LRG sample is obtained with lower limiting magnitude than the Main galaxy samples. We will use the continuous mass-bin samples to investigate the cosmological constraining power at each mass, but we will compare to the nine SDSS mass-bin samples (points) to make connections to the observations.

III. COMBINING GRAVITATIONAL LENSING AND GALAXY CLUSTERING

Large-scale galaxy clustering has been measured with high precision, and its theoretical interpretation is simple; it constrains the product of the matter fluctuation amplitude σ_8 and the bias of the galaxy sample. In this section, we take this con-

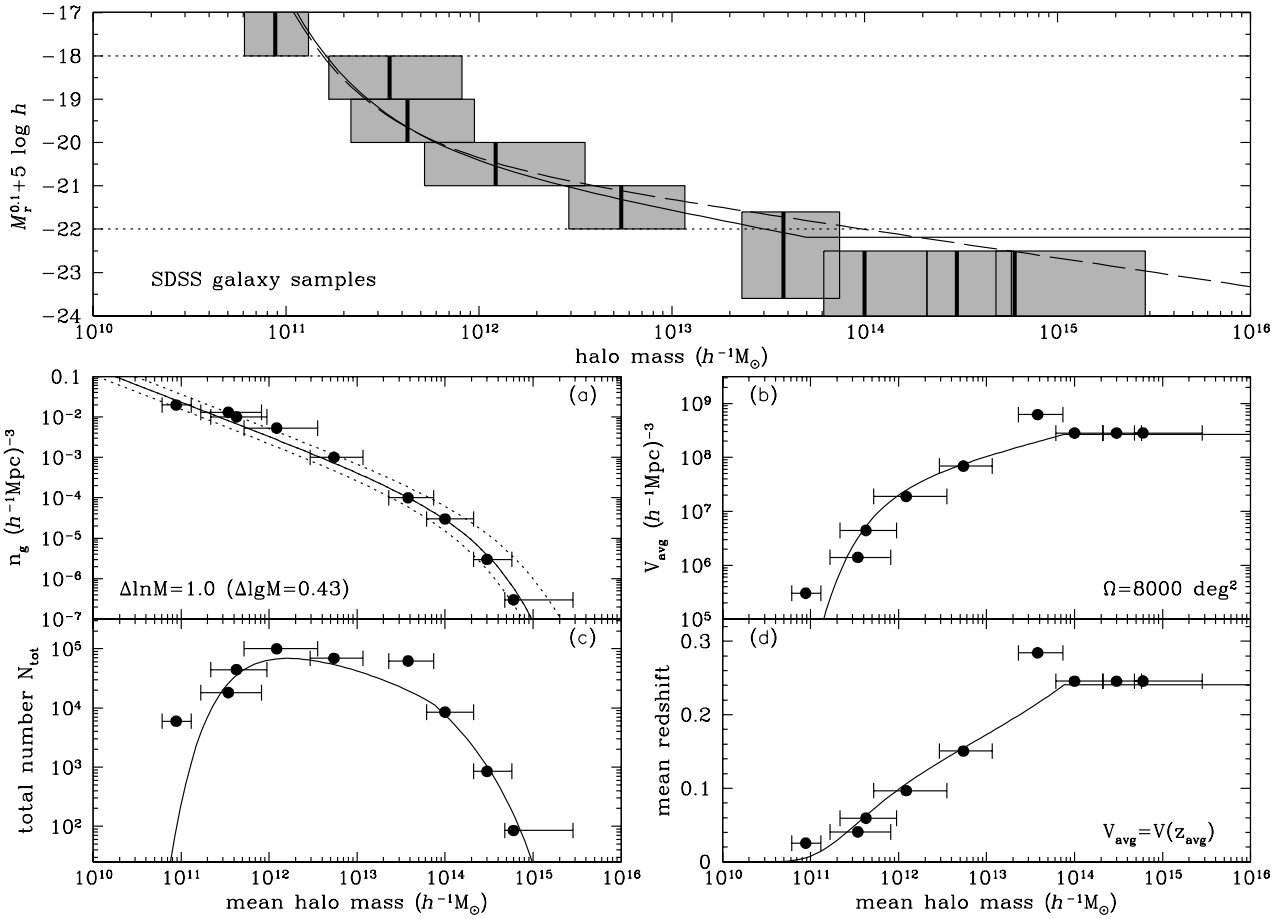

FIG. 1: SDSS galaxy and continuous mass-bin samples. We approximate galaxy samples as isolated halos and use the relation between central galaxy luminosity and halo mass to match the observed SDSS galaxy samples (discrete points, see Table I). Top panel: Rest-frame r-band magnitude at $z = 0.1$. Vertical solid lines show the mean mass of the SDSS galaxy samples obtained from the galaxy-galaxy lensing measurements [18, 31]. The minimum and the maximum masses represented by gray boxes are obtained by matching the mean mass and the number density of the SDSS galaxy samples. The dashed curve shows the mass-luminosity relation [30] between the central galaxy luminosity and its halo mass, obtained by analyzing the clustering measurements of the SDSS Main galaxy samples. Its validity is limited to $-22 \leq M_r^{0.1} + 5\log h \leq -18$ (horizontal lines). We modify the mass-luminosity relation shown as the solid curve to implement the LRG and the maxBCG samples at high luminosity, but account for the flattening of the luminosity of central galaxies at $M > 5 \times 10^{13} h^{-1} M_\odot$. Bottom panels: The average volume and the mean redshift of the SDSS galaxy samples are obtained by dividing the observed number density by the total number of observed galaxies. For the continuous mass-bin samples (solid), we adopt the mass-bin interval $\Delta \ln M$ (dotted) that closely matches the observed number densities of the SDSS galaxy samples, and we compute the average volume and the mean redshift by using the mass-luminosity relation.

straint from the large-scale clustering measurements of each galaxy sample as a base in our cosmological parameter analysis and combine various gravitational lensing measurements to derive further improvements on cosmological parameter constraints in a model-independent way. The abundance information is also considered in conjunction with its mass measurements from gravitational lensing.

To facilitate our understanding of these complementary approaches, we split the lensing measurements into two regimes (small-scale and large-scale) and call these two different ways method I and method II, respectively. We investigate in Secs. III B and III C what information each method can add to the cosmological constraining power. The constraints from the abundance information (method III) and from the full analysis (method IV) of gravitational lensing and galaxy clustering are discussed in Secs. III D and III E.

A. Large-Scale Galaxy Clustering

The signal-to-noise ratio of large-scale galaxy clustering measurements can be determined by the number of independent Fourier modes obtainable in a survey volume V_s probed by each galaxy sample. Using the standard mode counting method, we compute the signal-to-noise ratio of large-scale clustering measurements, accounting for the shot-noise and

the sample variance, as

$$\left(\frac{S}{N}\right)^2 = \frac{1}{2}\int_{k_{\rm min}}^{k_{\rm max}} \frac{dk}{k}\,\frac{4\pi k^3 V_s}{(2\pi)^3}\,\left[\frac{n_g P_0(k)}{1+n_g P_0(k)}\right]^2 , \quad (1)$$

where $k_{\rm min} = dk = 2\pi/V_s^{1/3}$ and a factor two accounts for the double counting of Fourier modes due to the reality of the galaxy fluctuation field. We modeled the redshift-space galaxy power spectrum on large scales using linear theory $P_0(k) = (1+2\beta/3+\beta^2/5)P_g(k)$ and $P_g(k) = b_g^2\,P_{\rm lin}(k)$, where $\beta = f/b_g$ and f is the logarithmic rate of growth.

Given the mass range ($M_{\rm min}$, $M_{\rm max}$) of the SDSS galaxy and the continuous mass-bin samples, the galaxy bias factor is

$$b_g = \frac{1}{n_g}\int_{M_{\rm min}}^{M_{\rm max}} dM\,\frac{dn}{dM}\,b(M)\,, \quad (2)$$

and the mean mass of the samples is

$$\bar{M} = \frac{1}{n_g}\int_{M_{\rm min}}^{M_{\rm max}} dM\,\frac{dn}{dM}\,M\,, \quad (3)$$

where the halo mass function dn/dM and its bias factor $b(M)$ are computed by using the Tinker et al. [69] and the Tinker et al. [70] fitting formulas, respectively.

Figure 2 illustrates the galaxy bias and the clustering constraints of the galaxy samples. We use Eq. (2) to model the galaxy bias factor of each sample. Bias is a monotonic function of mass and is rather flat in the low mass regime. While the SDSS galaxy samples (points) are at different mean redshifts, their bias factors largely agree with the bias factors of the continuous mass-bin samples at $z = 0.1$, as their redshift range is narrow $z = 0.1 - 0.3$.

The bottom panel shows the clustering constraint on the product $\mathcal{C} = b_g\sigma_8$ (note Eq. [1] is the signal-to-noise ratio on square of the product). Fainter galaxies (low mass halos) have lower shot-noise due to larger abundances, though the signal $\mathcal{C}$ is rather flat due to the constant galaxy bias at low mass. However, the volume probed by these faint galaxies is so small as seen in Figure 1 that there exist only few Fourier modes and hence the clustering constraint in Figure 2 is weak at low mass. Especially at low mass, the small volume probed by the faint galaxies sets the minimum wavenumber $k_{\rm min}$ close to the maximum wavenumber $k_{\rm max} = 0.1h{\rm Mpc}^{-1}$ we adopted, and thereby the clustering constraints at low mass are discrete and weak.

In the high mass regime, where the galaxy samples correspond to luminous galaxies and clusters, the galaxy bias factor continuously increases with mass, and so does the clustering signal $\mathcal{C}$. However, while the volume probed by the clusters is assumed constant (Fig. 1), the shot-noise of clusters dramatically increases at high mass due to the exponential nature of mass function, degrading the clustering constraints of very massive halos.

Given the volume probed by each galaxy sample and the ratio of their galaxy power spectrum to the shot-noise, the LRG sample yields the best clustering constraint. Dashed and dotted curves in Figure 2 demonstrates the sensitivity to the maximum wavenumber. For various values of $k_{\rm max}$, the trend of

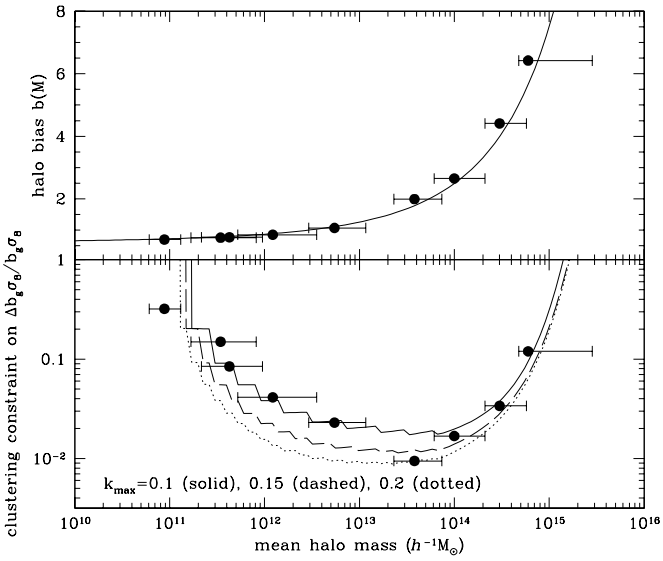

FIG. 2: SDSS galaxy bias and clustering constraints. Large-scale galaxy clustering measurements constrain the combination of the galaxy bias b_g and the matter fluctuation amplitude σ_8. For the fiducial cosmological model, two panels show the mean halo bias factor in Eq. (2) and the clustering constraints in Eq. (1), computed at the mean redshift for the SDSS galaxy samples (points) in Table I and at $z = 0.1$ for the continuous mass-bin samples (curves). The clustering constraints are insensitive to the choice of $k_{\rm min} = 2\pi/V_s^{1/3}$ but depend on the adopted value of $k_{\rm max}$. Due to small volume probed by less luminous galaxies, the clustering constraints are not smooth at low mass.

the clustering constraint in mass remains unchanged. While the clustering measurements are more precise in the nonlinear regime, its theoretical interpretation becomes more prone to systematic errors from nonlinear evolution.

B. Method I: Small-Scale Galaxy-Galaxy Lensing and Large-Scale Clustering

Galaxy-galaxy lensing measurements on small scales provide a robust and a model-independent way to estimate the mean mass of the galaxy samples. While the mean matter density Ω_m may not be well constrained by gravitational lensing alone, the mean mass is well constrained, as it is proportional to $\omega_m = \Omega_m h^2$. So we model two observable constraints, the large-scale galaxy clustering and the small-scale galaxy-galaxy lensing, by using three independent physical parameters: two cosmological parameters and the mean mass, $\mathbf{p} = (\Omega_m,\ \sigma_8,\ \bar{M})$.

The uncertainty in the mass measurements can be computed by adopting the Fisher information technique. Given the fiducial cosmological parameters, we first compute the total number $N_{\rm tot}$ of foreground lens galaxies shown in Figure 1 that will be stacked for galaxy-galaxy lensing measurements. As a function of angular separation θ from the lens galaxies, the total number of background source galaxies for shape mea-

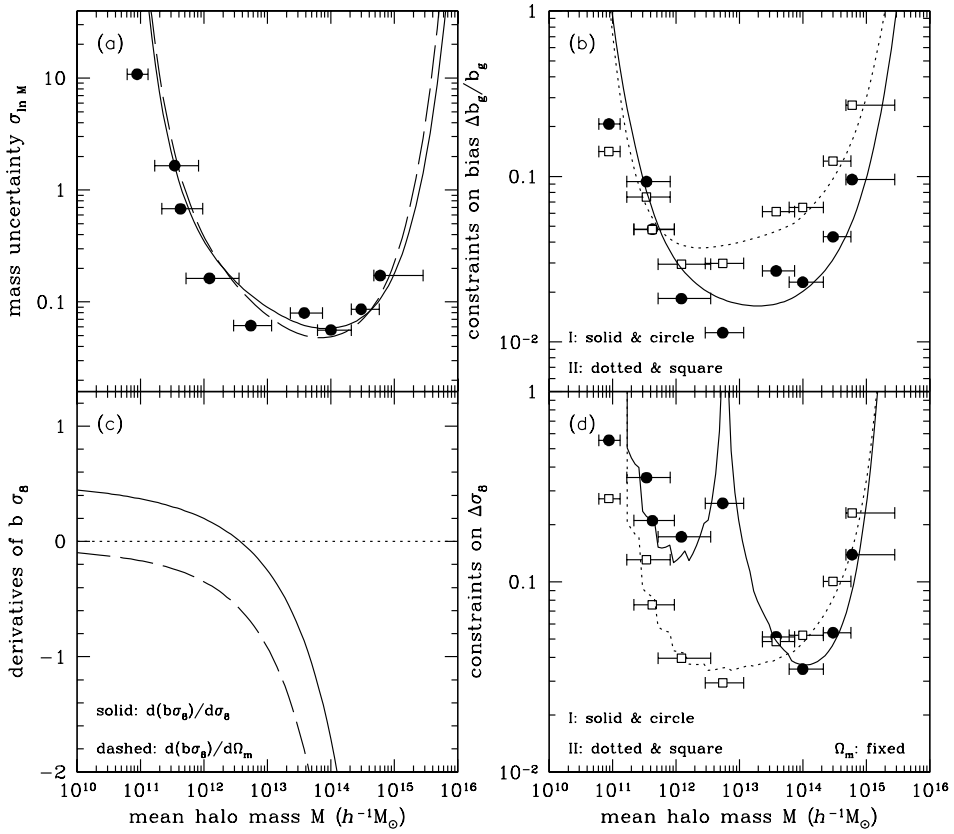

FIG. 3: Galaxy-galaxy lensing and large-scale clustering constraints. (a) Small-scale lensing measurements constrain the mean mass of the continuous mass-bin (solid) and the SDSS galaxy (points) samples. The mass uncertainties are derived by using the lensing measurements at projected separation $R_p = 0.2 \sim 2\ h^{-1}$Mpc, adjusted for each sample in proportion to $(M/M_0)^{1/3}$, where M_0 is the mean mass of the SDSS L4 sample. The dashed line shows the mass uncertainties without the mass-dependent adjustment in R_p. (b) Lensing constraints on galaxy bias, using the method I (solid & circles) and the method II (dotted & squares). The mass uncertainties are converted into uncertainties in galaxy bias (solid) by using the theoretical prediction of galaxy bias $b(M)$. Large-scale lensing measurements (dotted) directly constrain the galaxy bias factor of each sample, and the measurements constraints are derived by using the signals at $R_p = 3 \sim 60h^{-1}$Mpc. Remaining cosmological parameters are held fixed in both cases, including the mean matter density. (c) Cosmological parameter sensitivity of clustering constraint $\mathcal{C}$ in each mass. (d) Constraints on the matter fluctuation amplitude from galaxy-galaxy lensing and large-scale galaxy clustering.

surements is

$$N_{bg}(\theta) = N_{\rm tot}\ n_{bg}\ 2\pi\theta\Delta\theta\ , \tag{4}$$

where the number density of background source galaxies is $\bar{n}_{bg} = 1.2\,{\rm arcmin}^{-2}$ in the SDSS and we use only those galaxies behind the lens galaxies $z_s \geq z_l + 0.1$, i.e.,

$$n_{bg} = \bar{n}_{bg} \int_{z_l+0.1}^{\infty} dz\ \frac{dn_{bg}}{dz}\ . \tag{5}$$

The redshift distribution of background source galaxies is normalized, and we model it with three free parameters (a, b, c) as

$$\frac{dn_{bg}}{dz} = \frac{b\, c^{\frac{1+a}{b}}}{z_0 \Gamma\left(\frac{1+a}{b}\right)} \left(\frac{z}{z_0}\right)^a \exp\left[-c(z/z_0)^b\right]\ , \tag{6}$$

where $\Gamma(x)$ is the Gamma function. The mean redshift is

$$\bar{z} = \frac{z_0}{c^{1/b}} \frac{\Gamma\left(\frac{2+a}{b}\right)}{\Gamma\left(\frac{1+a}{b}\right)}\ , \tag{7}$$

and the median redshift can be obtained from

$$\gamma\left[\frac{1+a}{b}, c\left(\frac{z_{\rm med}}{z_0}\right)^b\right] = \frac{1}{2}\Gamma\left(\frac{1+a}{b}\right)\ , \tag{8}$$

by solving the incomplete Gamma function $\gamma(a, x)$. For the galaxy-galaxy lensing measurements in the SDSS, we adopt (a, b, c)=(1.34, 2, 1/2) with the mean redshift $\bar{z} = 1.38 z_0 = 0.42$ and the median redshift $z_{\rm med} = 1.31 z_0 = 0.40$ from [49].

The total number of background source galaxies determines the uncertainties in shear measurements

$$\sigma_\gamma^2(\theta) = \frac{\sigma_\gamma^2}{N_{bg}(\theta)} = \frac{1}{N_{bg}(\theta)} \left(\frac{\sigma_{\rm int}}{\mathcal{R}}\right)^2\ , \tag{9}$$

where the intrinsic shape noise is $\sigma_{\rm int} = 0.37$ and the responsivity is $\mathcal{R} = 1.7$ [18]. Note that these numbers are observables and held fixed for cosmological parameter variations.

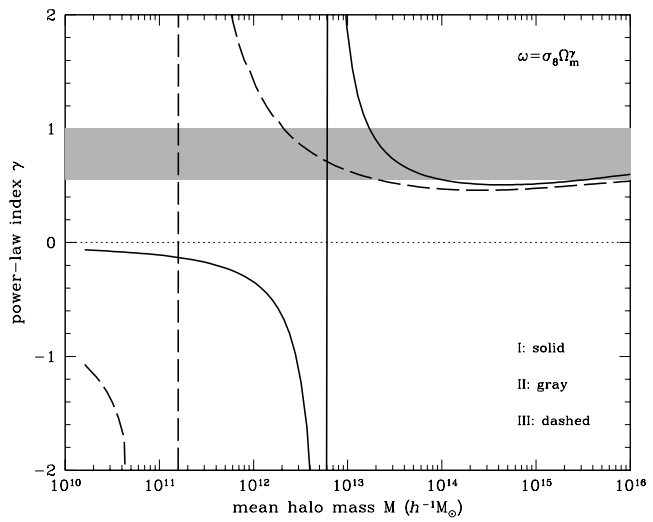

FIG. 4: Indices of the cosmological parameter constraints from three different methods of combining gravitational lensing and large-scale galaxy clustering (I: small-scale lensing, II: large-scale lensing, III: abundance). The clustering constraints in Fig. 2 are included in all three methods. Parameter indices are derived by using Eqs. (17) and (24). The value of γ in the method II depends on the smallest scale included in the analysis, and its range is plotted as a gray area.

Therefore, the uncertainties in the mass measurements are

$$\frac{1}{\sigma^2_{\bar{M}}} = \sum_\theta \frac{1}{\sigma^2_{\bar{\gamma}}(\theta)} \left[\frac{\partial\bar{\gamma}(\theta)}{\partial\bar{M}}\right]^2 , \qquad (10)$$

and the mean shear signal is computed by using the excess surface density $\Delta\Sigma$ of the foreground lens galaxy sample as

$$\bar{\gamma}(\theta) = \int_{z_l+0.1}^{\infty} dz_s \, \frac{dn_{bg}}{dz_s} \, \frac{\Delta\Sigma(\theta,\bar{M})}{\Sigma_c(z_l,z_s)} . \qquad (11)$$

where the (comoving) critical surface density is

$$\Sigma_c = \frac{c^2}{4\pi G} \frac{r_s}{r_l r_{ls}} \frac{1}{1+z_l} , \qquad (12)$$

and (r_l, r_s, r_{ls}) are the comoving angular diameter distances to the lens, the source, and between the lens and the sources, respectively. The factor $(1+z_l)$ arises due to our use of comoving angular diameter distances. The excess surface density $\Delta\Sigma(\theta, M)$ on small scales is computed by using the projected NFW density profile $\Sigma(R)$ [71, 72] as the difference $\Delta\Sigma = \bar{\Sigma}(<R) - \Sigma(R)$ between the mean surface density $\bar{\Sigma}$ interior to the disk and the surface density at the same projected radius $R = \theta r_l$.

Figure 3a shows the uncertainty $\sigma_{\ln\bar{M}}$ in the mass measurements of the galaxy samples. We limit the small-scale lensing measurements to the angle, corresponding to the projected separation $R_p = 0.2 \sim 2h^{-1}$Mpc to avoid complications due to the baryonic effects at the center. The angular range is set for the SDSS L4 sample and is adjusted for each sample in proportion to its virial radius $\propto M^{1/3}$. However, the impact of this adjustment is small (dashed). The uncertainty in the mass measurements is dominated by the total number $N_{\rm tot}$ of lens galaxies and hence the total number N_{bg} of background source galaxies. The LRG sample exhibits a weaker constraint $\sigma_{\ln\bar{M}}$ than the L5 or the maxBCG samples, slightly deviating from the trend shown in the continuous mass-bin samples (solid), because the mean redshift of the LRG is higher and there exist fewer background source galaxies for shape measurements.

Now, in order to combine the mass measurements $\bar{M}$ with the large-scale clustering constraints $\mathcal{C}$ and constrain the cosmological parameters, we perform an error propagation analysis:

$$d\mathcal{C} = \frac{\partial\mathcal{C}}{\partial\Omega_m} d\Omega_m + \frac{\partial\mathcal{C}}{\partial\sigma_8} d\sigma_8 + \frac{\partial\mathcal{C}}{\partial\bar{M}} d\bar{M} . \qquad (13)$$

With the matter density fixed ($\Delta\Omega_m = 0$), the constraint on σ_8 from the large-scale clustering and the small-scale galaxy-galaxy lensing measurements is

$$\Delta\sigma_8^2 = \left(\frac{\partial\mathcal{C}}{\partial\sigma_8}\right)^{-2} \left[\sigma^2_{\mathcal{C}} + \left(\frac{\partial\mathcal{C}}{\partial\bar{M}}\right)^2 \sigma^2_{\bar{M}}\right] , \qquad (14)$$

and this shows how sensitive the large-scale clustering $\mathcal{C}$ is to the change in the mean mass of the galaxy sample and the matter fluctuation amplitude.

The sensitivity to halo mass can be read off from Figure 2 as $\partial\mathcal{C}/\partial M = \sigma_8(\partial b_g/\partial M)$. Since the galaxy bias factor is a monotonic function of mass and it is nearly constant at low mass end, large uncertainty in mass for faint galaxy samples can only contribute little to the uncertainty in the galaxy bias factor. Figure 3b shows the uncertainty (solid) in bias prediction b_g constrained by using the small-scale lensing measurements of the mean mass. An order of magnitude uncertainty in mass for the SDSS L1−L3 samples translates into fairly good estimates of bias factors, while the galaxy bias factors are still better constrained for the luminous galaxy samples.

However, an accurate estimate of galaxy bias may be irrelevant in constraining the cosmological parameter if the product, the clustering constraint $\mathcal{C}$, is independent of the change in the matter fluctuation amplitude. Figure 3c plots the sensitivity to the fluctuation amplitude (solid) and to the mean matter density (dashed). A high peak of a density field becomes less biased as the rms fluctuation amplitude increases. Therefore, the sensitivity becomes negative at high mass, and there exists a zero-crossing in the derivative $\partial\mathcal{C}/\partial\sigma_8$, where the change in σ_8 is compensated by the change in b_g, leaving the clustering amplitude unchanged. At this mass the method I cannot give any cosmological constraints on the matter fluctuation amplitude σ_8.

Figure 3d illustrates the constraint (solid) on σ_8 from combining the large-scale clustering and the small-scale galaxy-galaxy lensing. The insensitivity of the clustering amplitude to the matter fluctuation amplitude is reflected as no constraint around $M \sim 5\times10^{12}h^{-1}M_\odot$. In [38] this method was applied to L4 and L5 galaxies, which we see are close to this

zero crossing where no information can be extracted. As a result, the derived constraints in [38] are relatively weak. The matter fluctuation amplitude can be best constrained by using the LRG or the maxBCG samples around $M \simeq 10^{14}h^{-1}M_{\odot}$. At high mass, the low number density n_g (and hence the total number $N_{\rm tot}$) is the dominant source of errors in measurements of the mean mass and the clustering amplitude of the galaxy samples. Since the theoretical prediction of the galaxy bias factor is based on lensing mass estimates and the galaxy-galaxy lensing measurements are obtained by averaging over all galaxies with different large-scale environments, the bias prediction is not subject to the sample variance errors and is little affected by the systematic errors due to the halo assembly bias (e.g., [73–75]). As long as nearly all halos at a given mass are included in the sample, the impact of the halo assembly bias is small.

With two observables $\mathcal{C}$ and $\bar{M}$, we can only constrain two parameters. To obtain constraints on the cosmological parameter combination, we define $\omega = \sigma_8^{\alpha}\Omega_m^{\gamma}$, and the propagation equation (13) is

$$d\mathcal{C} = \left(\frac{\partial \mathcal{C}}{\partial \Omega_m}\right)\frac{\Omega_m}{\gamma}\frac{d\omega}{\omega} + \frac{\partial \mathcal{C}}{\partial \bar{M}}\, d\bar{M}\ , \qquad (15)$$

where

$$\frac{d\omega}{\omega} = \frac{\gamma}{\Omega_m}\left(d\Omega_m + \frac{\alpha}{\gamma}\,\frac{\Omega_m}{\sigma_8}\, d\sigma_8\right) \qquad (16)$$

and the power-law indices satisfy

$$\frac{\gamma}{\alpha} = \frac{\Omega_m}{\sigma_8}\frac{\partial \mathcal{C}}{\partial \Omega_m}\left(\frac{\partial \mathcal{C}}{\partial \sigma_8}\right)^{-1}\ . \qquad (17)$$

Without loss of generality, we let $\alpha \equiv 1$, i.e., $\omega = \sigma_8\Omega_m^{\gamma}$.

Figure 4 shows the power-law index γ (solid) for the method I of combining the large-scale clustering and the small-scale lensing measurements. At low mass end, the constraint is insensitive to the mean matter density $\gamma \simeq 0$, as the clustering amplitude is independent of Ω_m (shown as the dashed line in Fig. 3c). The index becomes infinity, reflecting that there is no constraint on the matter fluctuation amplitude around the zero-crossing point. Finally, the combination of large-scale galaxy clustering and small-scale lensing yields constraints on $\omega = \sigma_8\Omega_m^{0.6}$ at high mass. The fractional uncertainty $\Delta\omega/\omega$ is equivalent to the fractional uncertainty $\Delta\sigma_8/\sigma_8$ (Fig. 3d) if the mean matter density is known, otherwise one can think of this method of constraining ω.

C. Method II: Large-Scale Galaxy-Galaxy Lensing and Large-Scale Clustering

Galaxy-galaxy lensing on large scales provides measurements of the galaxy-matter cross-correlation, and as shown in [25] and by combining it with galaxy clustering one constrains the parameter combination $\omega = \sigma_8\Omega_m^{\gamma}$ with the power-law index γ as a function of scales. On large scales $\gamma = 1$, while if one extends the method to nonlinear scales one finds $\gamma \sim 0.55$ down to $3 - 4h^{-1}{\rm Mpc}$ [76]. The power-law index of the parameter combination $\omega = \sigma_8\Omega_m^{\gamma}$ is thus between 0.55 and 1, depending on the smallest scale included in the analysis, as shown as the gray area in Figure 4. Here we simply use the linear theory for the method II, i.e., $\gamma = 1$, in which no modeling of the galaxy bias factor is involved (hence the method II is not subject to the halo assembly bias).

Similarly to the small-scale lensing constraint on mass, we perform a Fisher matrix calculation to obtain constraints $\sigma_{\mathcal{G}}$, where $\mathcal{G} = b_g\Omega_m\sigma_8^2$ is the dependence of the amplitude of galaxy-galaxy lensing on cosmological parameters. In this case the mean shear signal $\bar{\gamma}(\theta)$ in Eq. (11) is obtained by computing the excess surface density $\Delta\Sigma$ on large scales with linear theory cross-correlation $\xi_{gm} = b_g\,\xi_m$. The lensing signal is summed over the projected separation $R_p = 3 \sim 60h^{-1}{\rm Mpc}$ for all galaxy samples.

The dotted curve in Figure 3b shows the constraints on the galaxy bias factor b_g when the cosmological parameters are held fixed (or the constraints on the large-scale galaxy-galaxy lensing amplitude $\mathcal{G}$). The method II works well over a broad range of mass, and the constraint from the LRG sample is $\sim 8\%$, consistent with [76]. However, if we limit the lensing measurements to $R_p = 3 \sim 30h^{-1}{\rm Mpc}$ as the case for the SDSS Main samples, the statistical power would be reduced by a factor two, and the LRG sample is best suited for the method II.

The large-scale clustering constraints are combined with the large-scale galaxy-galaxy lensing constraints by propagating errors as

$$\begin{pmatrix} d\mathcal{G} \\ d\mathcal{C} \end{pmatrix} = \begin{pmatrix} \frac{\partial \mathcal{G}}{\partial \Omega_m} & \frac{\partial \mathcal{G}}{\partial \sigma_8} & \frac{\partial \mathcal{G}}{\partial \bar{M}} \\ \frac{\partial \mathcal{C}}{\partial \Omega_m} & \frac{\partial \mathcal{C}}{\partial \sigma_8} & \frac{\partial \mathcal{C}}{\partial \bar{M}} \end{pmatrix} \begin{pmatrix} d\Omega_m \\ d\sigma_8 \\ d\bar{M} \end{pmatrix}\ . \qquad (18)$$

With the matter density fixed ($\Delta\Omega_m = 0$), the constraint on σ_8 from the large-scale clustering and the large-scale galaxy-galaxy lensing measurements is

$$\Delta\sigma_8^2 = \left(\frac{\partial \mathcal{C}}{\partial M}\frac{\partial \mathcal{G}}{\partial \sigma_8} - \frac{\partial \mathcal{G}}{\partial M}\frac{\partial \mathcal{C}}{\partial \sigma_8}\right)^{-2}\left[\left(\frac{\partial \mathcal{G}}{\partial M}\right)^2\sigma_{\mathcal{C}}^2 + \left(\frac{\partial \mathcal{C}}{\partial M}\right)^2\sigma_{\mathcal{G}}^2\right]\ . \qquad (19)$$

Figure 3d presents the constraint (dotted) on σ_8 from combining the large-scale clustering and lensing measurements. The best constraints on the matter fluctuation amplitude can be obtained from a fairly broad range in mass, covering the SDSS L4 to the maxBCG samples. The method II constraints are comparable to the method I, but they differ in the mass scale that provides best constraints.

We note that our analysis includes only statistical errors and not systematics (see, e.g., [45–49]). For example, currently the dominating source of error is photo-z calibration and conversion from observed ellipticity to shear, which contribute a combined 5% error on the amplitude of galaxy-galaxy lensing signal in the latest SDSS analysis [76]. This would suggest that the amplitude cannot be measured to better than 5% accuracy with the current analysis pipeline (already comparable to the statistical errors in the SDSS), and hence the

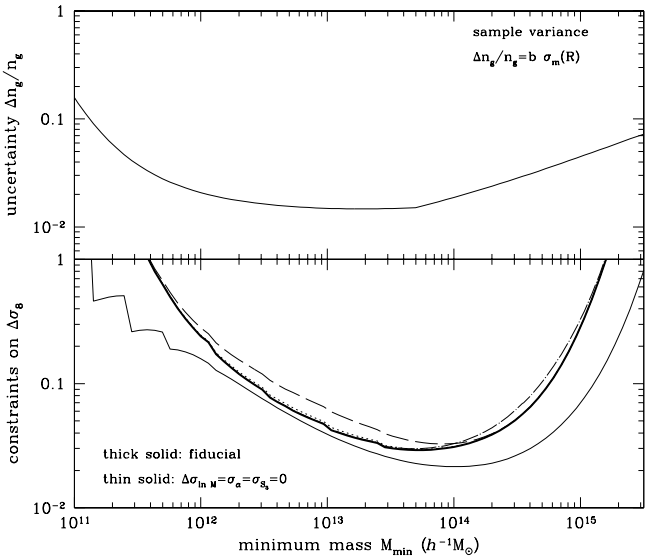

FIG. 5: Additional abundance constraints. Upper panel shows the sample variance in abundance due to the limited volume probed by the thresholded samples. Bottom panel shows the constraints on the matter fluctuation amplitude by adding additional abundance information. The mean mass and the clustering constraints are combined to constrain the minimum mass $M_{\rm min}$, the log-normal scatter $\sigma_{\rm lnM}$, and the matter fluctuation amplitude σ_8 (thick solid). We assume $\sigma_{\rm lnM}=0.5$ in the fiducial model. In addition, we consider two systematic errors: invisible halos and skewness ($S_3\neq 0$) in the mass-observable relation. If some fraction ($\alpha_g>0$) of halos are devoid of galaxies, they may drop out of the sample, acting as a systematic error. Dotted ($\sigma_{\alpha_g}=0.1$), dashed ($\sigma_{\alpha_g}=0.3$), and dot-dashed ($\sigma_{S_3}=5.0$) curves show the degradation in $\Delta\sigma_8$ due to systematic errors, if we marginalize over those parameters in our modeling. The constraint can be greatly improved (thin solid), if the log-normal scatter, the invisible fraction, and the skewness are perfectly known ($\Delta\sigma_{\rm lnM}=\Delta\alpha_g=\Delta S_3=0$).

constraint becomes inflated to $\Delta\sigma_8\sim 0.05$. The same systematic error would also apply to the shear-shear analysis, which results in $\Delta\sigma_8\sim 0.05$ in the linear regime and somewhat weaker systematic error $\Delta\sigma_8\sim 0.03$ in the quasilinear regime, as it scales as σ_8^3 [77]. However, an additional 5% shear-calibration uncertainty in the method I sets a floor at $\sim 7\%$ in mass measurements (since $M\sim\Sigma^{3/2}$), which degrades the σ_8-constraint to $\Delta\sigma_8\sim 0.04$. This suggests that method I is less sensitive to the overall calibration error than method II and shear-shear method. This may be an important consideration for the future surveys too.

D. Method III: Additional Abundance Information

Now we add the abundance information in the analysis and investigate its cosmological constraining power. Since the number density n_g of galaxy samples is rather sensitive to the mass-observable relation, we consider in this case thresholded galaxy samples, instead of luminosity-bin samples. As our fiducial model, we assume that the thresholded galaxy samples are described by two parameters, the minimum threshold mass $M_{\rm min}$ and the log-normal scatter $\sigma_{\rm lnM}$ of the mass-observable relation, given the cosmological parameters: $\mathbf{p}=(\Omega_m,\sigma_8,M_{\rm min},\sigma_{\rm lnM})$. We set $\sigma_{\rm lnM}=0.5$ in the fiducial model.

As our observables of the thresholded galaxy samples, we consider the abundance n_g of the galaxy sample, the mean mass $\bar{M}$ of the galaxy sample from small-scale lensing measurements, and the large-scale clustering $\mathcal{C}$: $\mathbf{O}=(n_g,\bar{M},\mathcal{C})$. The number density of the thresholded galaxy samples can be computed, accounting for the scatter in the mass-observable relation, as

$$n_g=\int_0^\infty dM\ \frac{dn}{dM}\ \frac{1}{2}\ {\rm erfc}\left[\frac{\ln M_{\rm min}-\ln M}{\sqrt{2}\sigma_{\rm lnM}}\right]\ , \qquad (20)$$

where ${\rm erfc}(x)$ is the complementary error function. The mean mass and the bias of the thresholded samples are then

$$\bar{M}\ =\ \frac{1}{n_g}\int_0^\infty dM\ M\ \frac{dn}{dM}\ \frac{1}{2}\ {\rm erfc}\left[\frac{\ln M_{\rm min}-\ln M}{\sqrt{2}\sigma_{\rm lnM}}\right] \qquad (21)$$

$$b_g\ =\ \frac{1}{n_g}\int_0^\infty dM\ b(M)\ \frac{dn}{dM}\ \frac{1}{2}\ {\rm erfc}\left[\frac{\ln M_{\rm min}-\ln M}{\sqrt{2}\sigma_{\rm lnM}}\right]\ .$$

We use the same mass-observable relation for the central galaxies of the thresholded samples as described in Figure 1, in computing the volume probed by the thresholded galaxy samples. Measurement uncertainties in the mean mass and the large-scale clustering amplitude are therefore obtained in the same way. While the measurement uncertainty in abundance is practically zero in observation, our theoretical prediction n_g in Eq. (20) is based on the globally averaged mass function, which differs from the measurements due to the sample variance (see, e.g., [78]). Therefore, we treat the sample variance in abundance as the measurement uncertainty σ_{n_g} in abundance, and for a galaxy sample covering the volume V the sample variance is computed as

$$\left(\frac{\Delta n_g}{n_g}\right)^2=\frac{\langle n_g^2\rangle-\bar{n}_g^2}{\bar{n}_g^2}=b_g^2\sigma_m^2(R)\ , \qquad (22)$$

where $R=(3V/4\pi)^{1/3}$ and $\sigma_m(R)$ is the rms matter fluctuation smoothed by a top-hat filter with R.

The upper panel in Figure 5 shows the fluctuation in the abundance $\Delta n_g/n_g$ due to the limited volume probed by the thresholded galaxy samples. As the volume coverage increases with the minimum threshold mass (or brighter galaxies), the sample variance decreases accordingly, and the observed abundance approaches to the global mean value to a percent level around $M_{\rm min}\sim 10^{14}h^{-1}M_\odot$. The upturn at $M>10^{14}h^{-1}M_\odot$ reflects the fact that the central galaxies of more massive clusters are not brighter, while they are more biased.

Using the matrix form between the observables $\mathbf{O}$ and the parameters $\mathbf{p}$, a general error propagation analysis can be performed as

$$d\mathbf{O}=\frac{\partial\mathbf{O}}{\partial\mathbf{p}}\ d\mathbf{p}\ , \qquad (23)$$

and assuming $\Delta\Omega_m = 0$ the constraint on σ_8 from the thresholded galaxy samples can be obtained as

$$\Delta\sigma_8^2 = \frac{1}{D^2}\left[\left(\frac{\partial\mathcal{C}}{\partial\sigma_{\rm lnM}}\frac{\partial\bar{M}}{\partial M_{\rm min}} - \frac{\partial\mathcal{C}}{\partial M_{\rm min}}\frac{\partial\bar{M}}{\partial\sigma_{\rm lnM}}\right)^2\sigma_{n_g}^2 + \left(\frac{\partial\mathcal{C}}{\partial\sigma_{\rm lnM}}\frac{\partial n_g}{\partial M_{\rm min}} - \frac{\partial\mathcal{C}}{\partial M_{\rm min}}\frac{\partial n_g}{\partial\sigma_{\rm lnM}}\right)^2\sigma_{\bar{M}}^2 + \left(\frac{\partial\bar{M}}{\partial\sigma_{\rm lnM}}\frac{\partial n_g}{\partial M_{\rm min}} - \frac{\partial\bar{M}}{\partial M_{\rm min}}\frac{\partial n_g}{\partial\sigma_{\rm lnM}}\right)^2\sigma_{\mathcal{C}}^2\right],$$

where the determinant of the matrix with $\mathbf{p} = (\sigma_8, M_{\rm min}, \sigma_{\rm lnM})$ is

$$D = \left|\frac{\partial\mathbf{O}}{\partial\mathbf{p}}\right| = \left(\frac{\partial n_g}{\partial\sigma_8}\right)\left(\frac{\partial\mathcal{C}}{\partial\sigma_{\rm lnM}}\frac{\partial\bar{M}}{\partial M_{\rm min}} - \frac{\partial\mathcal{C}}{\partial M_{\rm min}}\frac{\partial\bar{M}}{\partial\sigma_{\rm lnM}}\right) - \left(\frac{\partial\bar{M}}{\partial\sigma_8}\right)\left(\frac{\partial\mathcal{C}}{\partial\sigma_{\rm lnM}}\frac{\partial n_g}{\partial M_{\rm min}} - \frac{\partial\mathcal{C}}{\partial M_{\rm min}}\frac{\partial n_g}{\partial\sigma_{\rm lnM}}\right) + \left(\frac{\partial\mathcal{C}}{\partial\sigma_8}\right)\left(\frac{\partial\bar{M}}{\partial\sigma_{\rm lnM}}\frac{\partial n_g}{\partial M_{\rm min}} - \frac{\partial\bar{M}}{\partial M_{\rm min}}\frac{\partial n_g}{\partial\sigma_{\rm lnM}}\right).$$

The bottom panel in Figure 5 shows the constraint (thick solid) on σ_8 by adding the abundance information. Due to the exponential sensitivity, the derivatives of the abundance $\partial\ln n_g/\partial\ln\mathbf{p}$ are larger than the derivatives of the clustering amplitude and the mean mass, and the sample variance error in the abundance is always an order-of-magnitude smaller than the other uncertainties. Consequently, the uncertainties in the clustering amplitude and the mean mass dominate the error budget in $\Delta\sigma_8$ at all mass range, and the uncertainty in the matter fluctuation amplitude is set by the uncertainty in the clustering amplitude at high mass and the uncertainty in the mean mass at low mass.

Significant improvements (thin solid) can be made in constraining the matter fluctuation amplitude using the abundance information, if we have extra information about the log-normal scatter in the mass-observable relation. At a mass of $10^{14}h^{-1}M_\odot$ this leads to a factor of two improvement in the error. This shows the importance of knowing the scatter in the cluster abundance method. However, obtaining this scatter from other observations is difficult, since other observables have different distributions and associated scatters. Our approach of extracting it from the clustering is more conservative, as we discuss in more detail below. Though the constraints are still dominated by the uncertainties in the clustering amplitude and the mean mass, the sample variance becomes non-negligible in this limit. The power-law index of the parameter combination $\omega = \sigma_8\Omega_m^\gamma$ can be obtained by using the matrix form as

$$\gamma = \frac{\Omega_m}{\sigma_8}\frac{D\left[\mathbf{p} = (\Omega_m, M_{\rm min}, \sigma_{\rm lnM})\right]}{D\left[\mathbf{p} = (\sigma_8, M_{\rm min}, \sigma_{\rm lnM})\right]}, \qquad (24)$$

and Figure 4 shows the power-law index γ (dashed) for the method III. A unique signature is again there exist a mass range, where no constraint on the matter fluctuation amplitude can be derived ($\gamma \simeq \infty$). Since the change in the matter fluctuation amplitude results in not only the increase in the overall abundance of halos but also the distortion in the halos mass function, there exists a mass range $M \sim 10^{11}h^{-1}M_\odot$, at which no constraint on σ_8 can be obtained from the abundance. At high mass, the thresholded samples approach the mass-bin samples, and the constraints becomes $\omega \simeq \sigma_8\Omega_m^{0.6}$ as in the method I.

1. *Systematic Errors: Invisible Halos and Skewness in PDF*

Although the abundance information is a powerful tool to probe cosmology due to its exponential sensitivity at high mass, it is equally sensitive to systematic errors in theoretical modeling of the abundance. Here we consider two simple cases for potential systematic errors: Invisible halos and skewness in the probability distribution of the mass-observable relation. Invisible halos would appear to be a killer for this method, since with lensing and abundance information one would never be able to tell that some clusters are not present in the sample. However, with clustering information one can tell the difference. For example, if we assume for simplicity that there is no scatter then in a given model at a given abundance we measure all of the most massive halos at that abundance. If a fraction of these massive halos are dark, they are not in the catalog and need to be replaced with less massive halos to reach the same abundance. But these less massive halos also have lower bias, and the two cases can be distinguished if we include clustering information in addition to lensing and abundance. In this sense dark halos act in the same way as the scatter between mass and observable. Our goal in this subsection is to explore this in more detail to see if there is any residual difference between the two.

The first case is that some fraction α_g of halos at each mass fail to form galaxies and simply drop out of the observed galaxy samples. These invisible halos would act as a systematic error in our cosmological parameter analysis. In the presence of the invisible fraction, the halo mass function should be modified as $(1-\alpha_g)(dn/dM)$ in computing the number density in Eq. (20), while the mean mass and the bias factors in Eq. (21) remain unaffected. The effect of the invisible fraction on the mean mass and the bias factor arises solely from the change in $M_{\rm min}$, if the number density is held fixed.

The second case of systematic errors is a non-Gaussian probability distribution in the mass-observable relation. The thresholded galaxy samples are modeled by using the threshold mass $M_{\rm min}$ and the log-scatter $\sigma_{\rm lnM}$, assuming that the scatter between the observed mass and the true mass is a Gaussian. Now we consider a deviation from the Gaussian assumption. A non-Gaussian probability distribution function with known cumulants κ_n can be constructed by using a Gaussian distribution as [79]

$$P_{nG}(\delta) = \exp\left[\sum_{n=3}^{\infty}\frac{\kappa_n}{n!}\left(-\frac{d}{d\delta}\right)^n\right]P_G(\delta,\mu,\kappa_2), \qquad (25)$$

where the mean μ and the variance κ_2 of the Gaussian distribution are set equal to those in the non-Gaussian distribution.

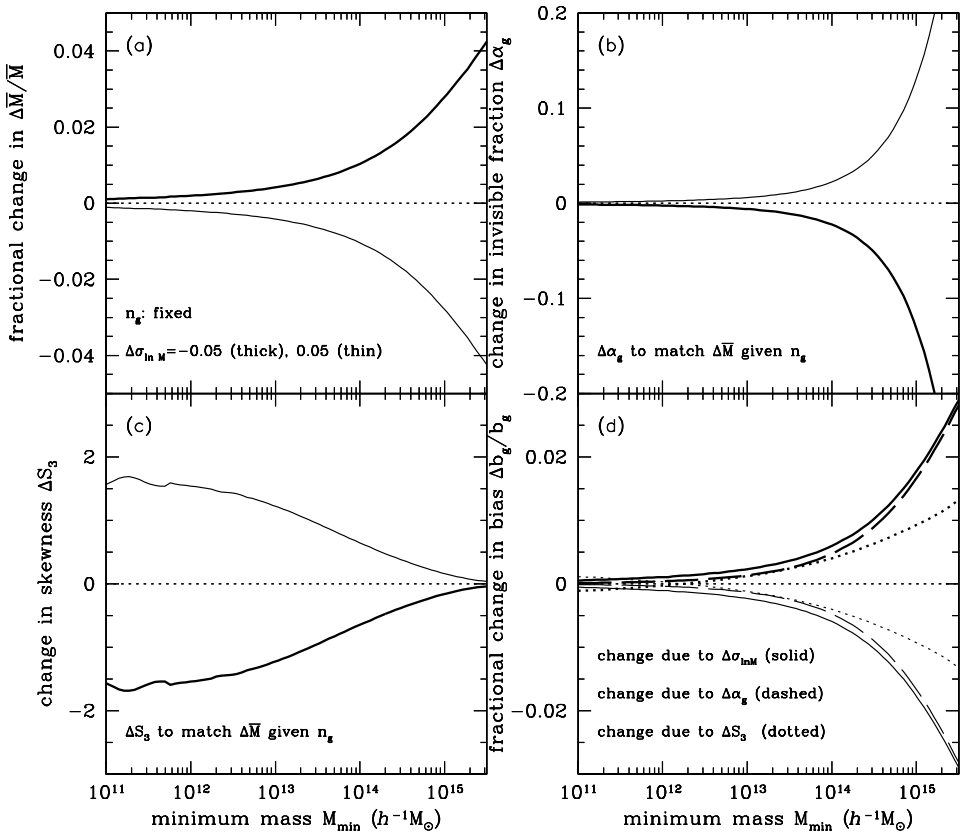

FIG. 6: Degeneracy in additional parameters of the thresholded samples. (a) The fractional change in the mean mass $\bar{M}$ due to the change in the log-normal scatter $\sigma_{\rm lnM}$. The minimum threshold mass $M_{\rm min}$ is adjusted to compensate for the resulting change in abundance in all panels, i.e., n_g is fixed as the value in the fiducial model. (b) The change in the invisible halo fraction α_g required to match $\Delta\bar{M}$ in Panel (a). While negative values of α_g are plotted for illustration purposes, only non-negative values of α_g have physical meaning. (c) The change in the skewness S_3 required to match $\Delta\bar{M}$ in Panel (a). The abundance is again fixed as in the fiducial model ($S_3 = 0$). (d) The fractional change in the galaxy bias factor due to the change $\Delta\sigma_{\rm lnM}$, $\Delta\alpha_g$, and ΔS_3 in each panel. The invisible fraction parameter α_g is largely degenerate with the log-normal scatter $\sigma_{\rm lnM}$, while the skewness S_3 is only degenerate below $M_{\rm min} < 10^{14}h^{-1}M_\odot$.

Using the Edgeworth expansion, we only keep the leading order correction to the Gaussian distribution,

$$P_{nG}(\delta) \simeq P_{\rm G}(\delta,\mu,\kappa_2)\left[1+\frac{\kappa_2}{6}S_3H_3\left(\frac{\delta}{\kappa_2}\right)\right], \qquad (26)$$

where the third-order Hermite polynomial is $H_3(x) = x^3 - 3x$ and the skewness is $S_3 = \kappa_3/\kappa_2^2$. In the presence of skewness ($S_3 \neq 0$), the change in the number density is therefore

$$\Delta n_g = \frac{S_3\sigma_{\rm lnM}}{12}\sqrt{\frac{2}{\pi}}\int_0^\infty dM\,\frac{dn}{dM}\left[\frac{(\ln M_{\rm min}-\ln M)^2}{\sigma_{\rm lnM}^2}-1\right] \times\exp\left[-\left(\frac{\ln M_{\rm min}-\ln M}{\sqrt{2}\sigma_{\rm lnM}}\right)^2\right], \qquad (27)$$

and similar calculations can be performed for the mean mass and the bias of the thresholded samples.

For intuitive understanding of the degeneracy between these additional parameters and the fiducial model parameters, we compute the change in our observables $\mathbf{O} = (n_g, \bar{M}, \mathcal{C})$, given cosmological parameters and the most well-measured abundance fixed. Figure 6a shows the fractional change in the mean mass $\bar{M}$ due to the change in log-normal scatter $\sigma_{\rm lnM}$. In order to compensate for the change in the abundance due to the increase in $\sigma_{\rm lnM}$, the minimum threshold mass $M_{\rm min}$ has to increase. However, the dilution of low mass halos results in decrease in the mean mass (thin solid). The impact is smaller at low $M_{\rm min}$ as the mass function flattens and the mean mass is dominated by $M \gg M_{\rm min}$.

Same effects can be achieved by introducing the invisible halo fraction $\alpha_g \neq 0$ or changing the skewness of the probability distribution $S_3 \neq 0$, without changing the log-normal scatter $\sigma_{\rm lnM}$. For a fixed abundance, the invisible halo fraction $\alpha_g > 0$ (thin solid) in Figure 6b needs lower minimum threshold mass and hence provides the same effect of reducing the mean mass. Since the magnitude of the change in α_g is directly proportional to the change in abundance, a fixed $\Delta\sigma_{\rm lnM}$ yields progressively small $\Delta\alpha_g$ at low mass.

A positive skewness (thin solid) in Figure 6c puts more weight on lower mass and brings more low mass halos into

the thresholded sample that mimicks the effect of the log-normal scatter on abundance. Similar to the log-normal scatter, the dilution of low mass halos decreases the mean mass. However, since thresholded samples are used, the change in the probability distribution affects the samples significantly at high mass, but little at low mass. Therefore, the degree of change allowed for the skewness can be large $|S_3\sigma_{\rm lnM}| > 1$, especially at low threshold mass.

Figure 6*d* illustrates the level of degeneracy of these additional parameters. For a fixed abundance, while the change in the mean mass can be masked by the change α_g or S_3, the change in the galaxy bias factor responds in a different way. The invisible fraction (dashed) is largely degenerate with the change (solid) in the log-normal scatter, such that the invisible halo fraction needs to be constrained to the level seen in Figure 6*b*. While the skewness (dotted) in the probability distribution yields somewhat different effects, the hyper-sensitivity to S_3 at high mass puts a very stringent requirements on S_3.

The impact of these systematic errors on the σ_8-constraint is presented in Figure 5. The fiducial model assumes no invisible halos ($\alpha_g = 0$) or skewness ($S_3 = 0$). However, with incomplete knowledge on the invisible halo fraction α_g or the skewness S_3, we marginalize over each of these parameters, and the constraint is inflated: $\sigma_{\alpha_g} = 0.1$ (dotted), $\sigma_{\alpha_g} = 0.3$ (dashed), $\sigma_{S_3} = 5.0$ (dot-dashed). This demonstrates the level of constraints on α_g and S_3 required to avoid a significant degradation on $\Delta\sigma_8$. As shown in Figure 6, the impact of the skewness is larger at high mass, and the impact of the invisible fraction is larger at low mass, but neither are very important at this level of precision, although they may become more important for the future data sets. Since the method III is essentially based on the method I, the same argument applies to the method III, regarding the halo assembly bias: provided that all halos of a given mass are included in the sample, the systematic errors due to the halo assembly bias should be minimal. Moreover, the assembly bias effect is small at high mass.

E. Combined Analysis of Galaxy-Galaxy Lensing and Large-Scale Clustering

For easy comparison of various methods for combining galaxy-galaxy lensing and galaxy clustering, Figure 7 summarizes the constraints on the matter fluctuation amplitude derivable from the SDSS galaxy samples. The constraint (thin solid) from the method III appears different from that in Figure 5, as it is plotted in terms of the mean mass of the galaxy samples, rather than the minimum mass. Since the method III makes use of the mass measurements in addition to the abundance information, it is effectively built upon the method I. Therefore, the constraints (thin solid) of the method III encompass the constraints (dashed) of the method I, although little difference arises due to the difference between the thresholded and the mass-bin samples, especially at low mass.

The dot-dashed curve shows the combined constraints of the large-scale galaxy clustering and the galaxy-galaxy lensing on all scales (method I and II). The constraints are obtained by adding the constraints from both methods in inverse quadrature. In this way, the large-scale clustering constraints in both methods are doubly counted. However, since the uncertainty in the clustering measurements is smaller than that in the lensing measurements in method II on large scales (and vice versa on small scales) and this trend is reversed in method I, the double counting of large-scale clustering constraints affects the final constraints little.

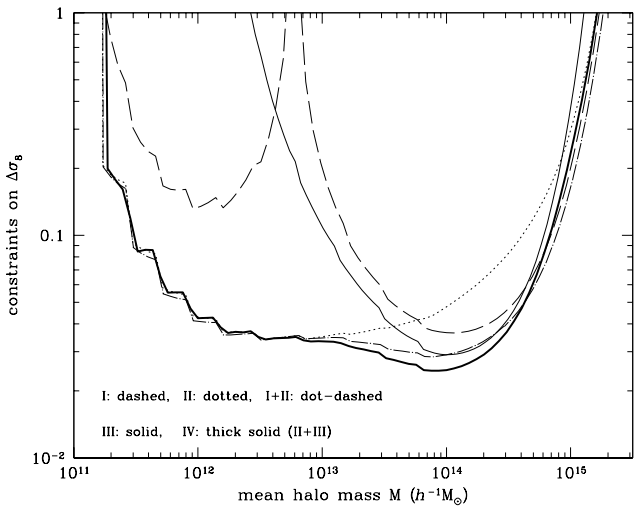

FIG. 7: Constraints on the matter fluctuation amplitude. Various curves show as a function of the mean mass of each sample, the constraints on $\Delta\sigma_8$ from three different methods (I, II, III). The dot-dashed curve shows the combination of method I and II, representing the constraints by combining the gravitational lensing on all scales and the large-scale clustering. The thick solid curve (method IV) shows the constraints by adding the abundance information to the gravitational lensing and the large-scale clustering constraints.

While the method III (solid) provides the best constraints among the three different methods, the combination of galaxy-galaxy lensing and large-scale clustering measurements (method I+II: dot-dashed) provides equally strong constraints, while it is less subject to systematic errors that may be present in the method III. Finally, all three methods can be combined, representing the full constraints (thick solid) by using the galaxy-galaxy lensing and large-scale clustering measurements. Compared to the method I+II, the abundance can bring additional information and tighten the constraints, albeit not much, around the mass range from the SDSS L4 to the maxBCG samples.

IV. FUTURE GALAXY SURVEYS

Here we extend our analysis performed in Sec. III to future galaxy surveys like the DES[1], BigBOSS[2], Euclid[3], and

[1] http://www.darkenergysurvey.org
[2] http://bigboss.lbl.gov
[3] http://sci.esa.int/euclid

TABLE II: Specifications of the future galaxy surveys adopted for forecasts. The sky coverage $\Omega_{\rm survey}$ is in units of square degrees, and the clustering measurements are assumed to be at the mean redshift $z_{\rm cl}$. The limiting magnitude is $m_{\rm lim}$ in r-band, and the intrinsic shear noise is σ_γ. The mean number $\bar{n}_{bg}$ of background source galaxies is per arcminute squared, and the redshift distribution parameters $(a, b, c, z_{\rm med})$ of the background source galaxies are described in Eq. (6). The last column indicates if the surveys are equipped with spectroscopic redshift measurements.

Survey	$\Omega_{\rm survey}$	$z_{\rm cl}$	$m_{\rm lim}$	$\bar{n}_{bg}$	σ_γ	a	b	c	$z_{\rm med}$	spec-z
SDSS	8000	0.1	22.5	1.2	0.22	1.34	2	1/2	0.4	Y
DES	5000	0.5	24.0	12.0	0.20	2.0	1.5	1	0.8	N
DES+BigBOSS	1000	0.5	24.0	12.0	0.20	2.0	1.5	1	0.8	Y
Euclid	20,000	0.7	24.0	40.0	0.20	2.0	1.5	1	1.0	Y
LSST	18,000	0.9	27.0	45.0	0.20	2.0	1.5	1	1.3	N

the LSST[4], and we forecast constraints derivable from these future surveys by combining galaxy clustering and gravitational lensing measurements. Compared to our previous investigation of the SDSS, the key difference is that these galaxy surveys have significantly lower threshold in flux, and they can observe fainter galaxies, thereby probing larger volume at higher redshift and providing higher statistical constraining power.

In addition to these simple scaling changes, two quantitative differences arise in the future galaxy surveys. Photometric surveys like the DES and the LSST will have a limited capability to map the galaxy positions in three dimensional space. Provided that there exist a small number of galaxies with spectroscopic redshift measurements for photometric redshift calibration, galaxy-galaxy lensing analysis can be performed without much degradation, compared to the surveys with full spectroscopic capacity. However, a full three-dimensional analysis of galaxy clustering will be unavailable in these photometric surveys. Moreover, we consider a hypothetical deep-imaging and spectroscopic survey over 1000 deg^2, which may be available from the overlapping region of the DES and the BigBOSS. This combination may allow for both gravitational lensing and galaxy clustering analyses. The BOSS and the BigBOSS alone are not considered here as they are mainly spectroscopic surveys without imaging and hence there are too few background source galaxies for gravitational lensing analysis in these surveys.

The other difference in the future surveys and possibly the major improvement over the SDSS is the availability of the cosmic shear measurements. A large number of background source galaxies in the future surveys enable high precision measurements of the shear-shear auto-correlation, which have been measured only in a very limited region of deep imaging in the SDSS [57–59]. In this section, we account for these changes by using the galaxy angular power spectrum in computing the clustering constraints for photometric surveys and by comparing the improved constraints in the future surveys to those derivable from the cosmic shear measurements. Table II summarizes the specifications of the future galaxy surveys we adopt in this paper.

[4] http://www.lsst.org

A. Combining Galaxy-Galaxy Lensing and Large-Scale Galaxy Clustering

While it is difficult to know which galaxy samples with what properties will be measured in the future surveys, it matters little to our present purposes of using them for gravitational lensing and galaxy clustering measurements. Here we approximate the galaxy samples in the future surveys as the mass-bin halo samples and compute the physical quantities plotted in Figure 1. The number density n_g of the galaxy samples is computed by adopting the same mass-bin interval $\Delta \ln M = 1.0$ as in the SDSS, but the resulting number density in the future surveys is lower at high mass, as the mass function is computed at higher redshift $z_{\rm cl}$ described in Table II.

We use the same SDSS relation between the central galaxy luminosity and its halo mass as in Figure 1a (solid) to compute the mean luminosity distance that these galaxy samples can be measured in the future surveys. The mean luminosity distances are larger for the galaxy samples in the future surveys than those with the same absolute luminosities (or the same masses) in the SDSS, because the limiting flux $f_{\rm lim}$ is lower in the future surveys. The average volume probed by the galaxy samples is therefore $V_{\rm avg}(z) \propto f_{\rm lim}^{-3/2}/(1+z)^3$, where the limiting flux is related to the limiting magnitude $m_{\rm lim} = -2.5 \log_{10} f_{\rm lim} + m_0$ with additive constant m_0. We compute the mean luminosity distances and the average volumes for each sample in the future surveys by scaling those quantities in the SDSS. We can then readily obtain the total number $N_{\rm tot}$ and the mean redshift $\bar{z}$ of the galaxy samples in the future surveys.[5]

For photometric surveys like the DES and the LSST, we compute the signal-to-noise ratio of the angular clustering measurement, similarly to Eq. (1), but accounting for the lack

[5] We note that the limiting magnitudes of the future surveys in Table II represent those for the photometric imaging, and those for the spectroscopic measurements are shallower. However, since they are scaled with the SDSS, we suspect no substantial difference in our projection. More importantly, our projection for the future surveys should be taken with caution, as many uncertain factors can affect the results presented here.

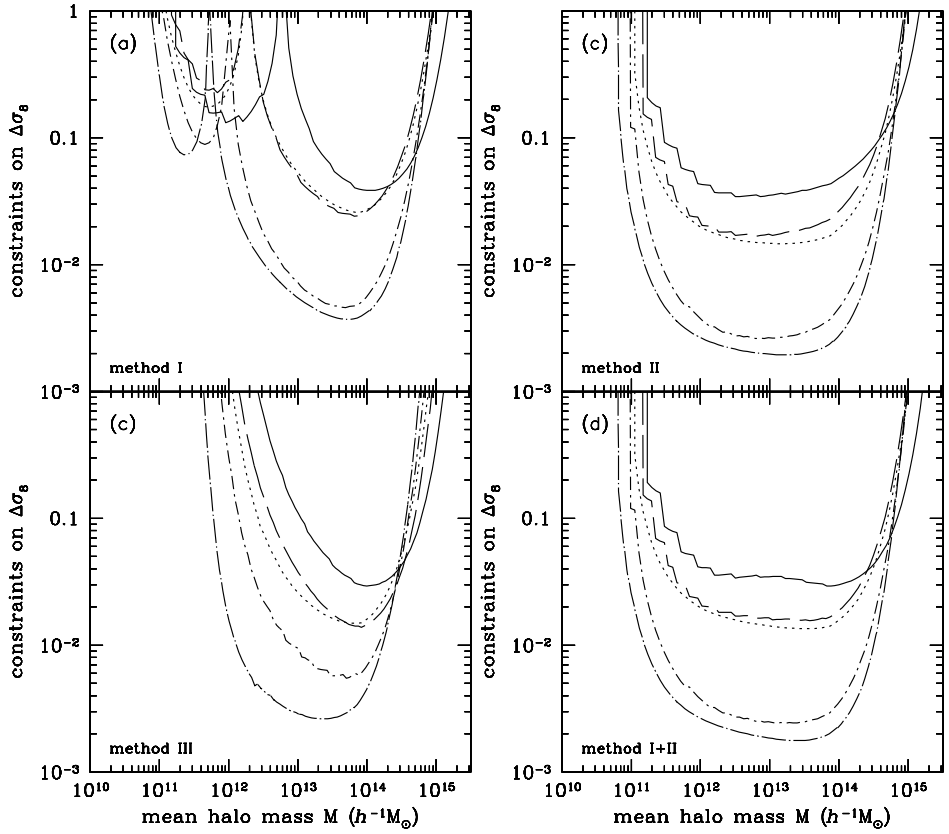

FIG. 8: Improvements of combining the large-scale galaxy clustering and the galaxy-galaxy lensing (methods I, II, III, and I+II) on the σ_8-constraints in future galaxy surveys. Each galaxy survey is indicated by various curves: SDSS (solid), DES (dotted), DES+BigBOSS (dashed), Euclid (short dot-dashed), and LSST (long dot-dashed). Compared to the SDSS (solid), the major improvements of the future galaxy surveys result from the larger survey volume at higher redshift. The specifications of the future galaxy surveys are summarized in Table II.

of three-dimensional information as

$$\left(\frac{S}{N}\right)^2 = \sum_{l=l_{\rm min}}^{l_{\rm max}} (2l+1)\frac{f_{\rm sky}\Delta l (C_l^g)^2}{2\left[C_l^g + C_l^n\right]^2}\,, \qquad (28)$$

where $f_{\rm sky}$ is the fraction of the sky covered by the survey and the noise power spectrum is $C_l^n = 4\pi f_{\rm sky}/N_{\rm tot}$. Adopting the Limber approximation and assuming that the galaxy samples are uniformly distribution in a narrow redshift range $z_{\rm cl} \pm \Delta z$, we compute the galaxy angular power spectrum as

$$C_l^g = \int dz\, \frac{H(z)}{r^2}\left(\frac{dn_g}{dz}\right)^2 P_g(k) = \frac{1}{r^2\Delta r} P_g\left(k=\frac{l}{r}\right)\,, \qquad (29)$$

where Δr is the width of the redshift bin $\Delta z = 0.05$. To be consistent with our calculations in spectroscopic surveys, the range of the angular multipoles in Eq. (28) is obtained by using the Limber relation $k = l/r$, given the range of wavenumber ($k_{\rm min}$, $k_{\rm max}$). In addition, we adopt $k_{\rm max} = 0.15h{\rm Mpc}^{-1}$ to take advantage of the fact that the structure probed by the future surveys remains in more linear regime than that probed by the SDSS.

Figure 8 describes the improvements of the matter fluctuation constraints over the SDSS by using the three different methods of combining the large-scale galaxy clustering and the galaxy-galaxy lensing measurements in various future surveys (different curves). The key improvements result from the larger survey volume and the larger number of background source galaxies at higher redshift, although the reduced number density increases the shot noise contribution.

Figures 8a and 8b show the constraints on σ_8 by combining the large-scale clustering and the galaxy-galaxy lensing measurements on small and large scales, respectively. In addition to the improvements in the clustering constraints, a larger number density of background source galaxies at higher redshift enables higher precision lensing measurements in the future surveys. Indeed, the contribution of the clustering constraints in the method II are weaker than the contribution of the large-scale galaxy-galaxy lensing constraints, whereas in the SDSS the trend is opposite. However, in the method I the contribution of the small-scale galaxy-galaxy lensing constraints is weaker, as the bias factor is highly constrained due to its flat nature at low mass and hence the improvements in bias estimates are gradual even with substantial improvements in mass measurements of the galaxy samples.

The situation is similar for the method III, shown in Figure 8c, to the case in the SDSS. As more volume is available,

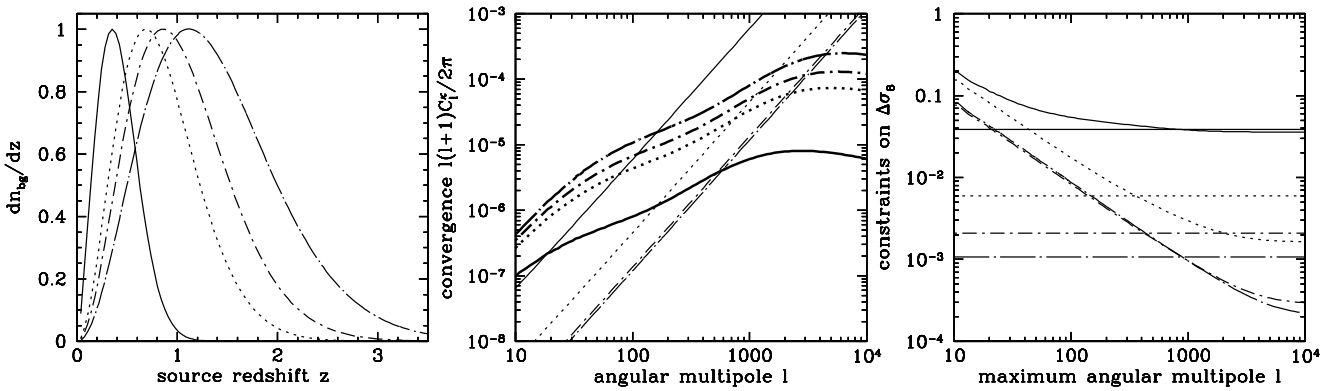

FIG. 9: Constraints on the matter fluctuation amplitude from the cosmic shear measurements in future surveys. Various curves represent different galaxy surveys as in Figure 8 and Table II: SDSS (solid), DES (dotted), Euclid (short dot-dashed), and LSST (long dot-dashed). *Left:* The redshift distribution of the background source galaxies. *Middle:* The angular convergence power spectrum (thick) and the noise power spectrum (thin). *Right:* The constraints on the matter fluctuation amplitude as a function of the maximum angular multipole. For comparison only, we included the SDSS (solid) for the cosmic shear measurements, although it is hard to measure in the SDSS. Horizontal lines represent the non-Gaussian contributions of the lensing trispectrum and the sample variance [80–82], both of which dominate the error budget on small scales.

the sample variance in abundance decreases even further in the future surveys, making the uncertainties in the number density nuisance. Consequently, the uncertainties in the clustering amplitude and the mean mass are the dominant factors in $\Delta\sigma_8$ at all mass range, even though the lensing constraints in the mass measurements improve more than the clustering constraints, compared to the SDSS. The best constraints on the matter fluctuation amplitude in the future surveys are achieved at slightly lower mass than in the SDSS, since much fewer galaxies at high mass are available at high redshift than at low mass, relatively.

All of the three methods dramatically improve the constraints on the matter fluctuation amplitude over the SDSS, promising sub-percent level measurements. While the method III has somewhat better statistical power in the SDSS than the method I or II, its statistical power is comparable to other methods in the future surveys and is *not* superior to the combined method I+II in Figure 8*d*. While no systematic errors are considered in Figure 8, they are relatively well known for the methods I and II. The systematic errors we considered for the method III in Sec. III D 1 are relatively innocuous, but the method III may be subject to other unknown systematic errors, which may become dominant when the overall constraints reach the sub-percent level in precision.

B. Cosmic Shear Power Spectrum from Gravitational Lensing

In addition to the measurements of galaxy clustering and galaxy-galaxy lensing, the future galaxy surveys have a large number of background galaxies at high redshift enough to provide robust measurements of cosmic shear signals. Here we compute constraints on the matter fluctuation amplitude by using the cosmic shear measurements in the future surveys and compare them to the constraints described in Sec. IV A.

The shapes of background source galaxies are subtly distorted by the foreground matter distribution, and the statistical measurements of the background galaxy shapes can be used to isolate the distortion from their intrinsic shapes. These cosmic shear signals measured by the distortion in shapes are represented by the projected matter fluctuation, or the convergence κ. Using the Limber approximation we compute the convergence power spectrum as

$$C_l^\kappa = \int_0^\infty dz\, W^2(z)\, P_m\left(k=\frac{l}{r};z\right)\,, \qquad (30)$$

where the weight function is

$$W(z) = \frac{3H_0^2}{2}\,\frac{\Omega_m}{a}\int_z^\infty dz_s\,\frac{dn_{bg}}{dz}\,\frac{r(z_s,z)}{r(z_s)}\,. \qquad (31)$$

Here we consider different parameters for the background source distribution in Eq. (6) that are more adequate for higher redshift surveys than in the SDSS: $a = 2$ and $b = 1.5$. The median redshifts of the source galaxies in each survey are listed in Table II. To derive the constraints from the cosmic shear measurements, we compute the Fisher matrix [47, 83]

$$F_{\alpha\beta} = \sum_{l=2}^{l_{\rm max}}(2l+1)\frac{f_{\rm sky}\Delta l}{2\left[C_l^\kappa + C_l^n\right]^2}\frac{\partial C_l^\kappa}{\partial p_\alpha}\frac{\partial C_l^\kappa}{\partial p_\beta}\,, \qquad (32)$$

where the noise power spectrum in this case is $C_l^n = \gamma_{\rm int}^2/\bar{n}_{bg}$.

A few caveats are in order, regarding our forecasts of the cosmic shear measurements. Equation (32) accounts for the galaxy shape noises as the sole source of errors, while it is known that there exist numerous systematic errors associated with the instruments [45, 46], the photometric redshift measurements [49, 83], and the intrinsic alignments [48]. Our optimistic assumption should serve as the best possible constraints derivable by using the cosmic shear measurements.

Furthermore, while tomographic measurements of the cosmic shear signals at different redshift bins can improve constraints on the dark energy equation-of-state or its time evolution (e.g., [23]), we consider only a single redshift bin for cosmic shear measurements in the future surveys, since the information contents on the matter fluctuation amplitude should be the same as those obtained by using multiple tomographic bins.

The left panel of Figure 9 shows the redshift distributions of background source galaxies in the future surveys. While the redshift distribution parameters (a, b, c)=$(2, 1.5, 1)$ are different from those in the SDSS, the shape itself (various curves) is similar to each other, and only the median redshifts differ for various future surveys, as listed in Table II. The middle panel shows the convergence power spectrum C_l^κ (thick) and its noise power spectrum C_l^n (thin) from the cosmic shear measurements. With few background galaxies in the SDSS, the convergence power spectrum (solid) is dominated by the noise power spectrum, already at $l > 20$, though there exist $(2l + 1)$ modes to be added per each angular multipole. The convergence power spectra in the future surveys are larger than in the SDSS, since the background source galaxies are at higher redshift. The noise power spectra are smaller, simply due to larger number density in the future surveys.

The right panel shows the σ_8-constraints using the cosmic shear measurements as a function of the maximum angular multipoles. The σ_8-constraints improve as more modes are included, but they saturate, once the noise power spectrum overwhelms the convergence power spectrum. In our most optimistic consideration, the cosmic shear measurements will provide amplitude constraints from the future surveys that are well below 0.1%. It would appear that the cosmic shear measurements in the future surveys trump the previous three methods in constraining the matter fluctuation amplitude, if all the systematic errors are under control and full statistical powers are utilized as we assumed here. This is mostly a consequence of the fact that cosmic shear measurements can extract useful information on the dark matter clustering well into the nonlinear regime at high angular multipole l.

However, there are caveats to this conclusion. One is that baryonic effects also change the predictions at high l, and these would need to be understood in detail [84]. Second caveat is that there exist a sample variance and a nonlinear contribution of the matter trispectrum to the covariance of the lensing power spectrum on small scales [80–82]. High degree of correlations between modes implies no further information can be extracted from the lensing power spectrum on smaller scales. In the right panel of Figure 9, the horizontal lines show these contributions to the lensing measurement uncertainties in the matter fluctuation amplitude in future surveys. We find that most of the experiments saturate the useful information, long before they run out of signals, and the constraints from the cosmic shear measurements are comparable to those from the combined method I+II.

V. DISCUSSION

Cosmological methods in large-scale structure are traditionally divided into weak lensing, galaxy clustering, and cluster abundance. While they are usually presented as separate techniques, there exists a considerable overlap between three methods. For example, the cluster abundance method cannot exist without a proper cluster-mass calibration and it is widely accepted that mass calibration based on weak lensing is required [85]. This combines cluster abundance and weak lensing. Second, a nuisance parameter in cluster abundance method is the scatter between cluster observable, such as luminosity (in optical, X-ray or SZ), and the cluster mass. This scatter can in principle be determined from external data [65, 86], but it is not clear that such an approach is reliable. A more conservative approach is to determine scatter internally from the clustering amplitude [39, 40, 87]. This method thus combines lensing, clustering and counting (abundance). It is useful to ask the questions such as what is the mass range where we get most of the information, how can we combine the information from different mass ranges, what happens if we drop individual observations etc. The purpose of this paper was to address these questions.

The Sloan Digital Sky Survey (SDSS) has enabled high precision measurements of galaxy clustering and gravitational lensing for various galaxy samples that cover a wide range of halo masses, so we started our analysis with the SDSS. With careful modeling of the SDSS galaxy samples, we have examined the cosmological constraining power that is contained in each galaxy sample and can be derived by combining both measurements of galaxy clustering and gravitational lensing. Furthermore, we have extended our analysis to other ongoing and future galaxy surveys with larger volumes at higher redshifts such as the DES, Euclid, and the LSST. Our joint analysis of gravitational lensing and galaxy clustering provides a guidance to observational applications and planning future large-scale galaxy surveys. However, in doing the analysis we had to make a number of simplifying assumptions, so our results should be considered as a useful guidance rather than conclusive.

We have investigated the cosmological constraining power in three model-independent ways to gain physical insights of its information contents, using constraints on the amplitude of the dark matter power spectrum as the figure of merit. The first method [38] is based on the theoretical prediction of the relation between the halo mass and the bias factor (e.g., [70, 88–91]). While the large-scale clustering measurements provide only the relative bias, galaxy-galaxy lensing measurements on small scales can provide robust estimates of the mean mass of the galaxy samples. The theoretical prediction of galaxy bias can in principle be refined to arbitrary accuracy by using numerical simulations, and its predictions depend on cosmology. Comparison of its prediction based on the lensing measurements of mass to the clustering measurements then determines the acceptable sets of cosmological parameters. This method works best at relatively high masses corresponding to the LRG sample or small clusters, at which the mass-dependence of the bias function on cosmology is strong and the uncertainties

in mass measurements are smallest due to their large volume coverage and high mass. Moreover, this method can be easily extended to the future surveys without much difficulty in theory and observation. The main observational systematic issue related to the method are the centroiding issue, which can be ameliorated if one uses lensing statistics that do not use small scale lensing information [20]. On the other hand, we have shown that this method suffers less from the overall lensing calibration error than the other weak lensing based methods. The method also assumes that the halo bias depends on the halo mass only. This is true by definition if all the halos in a certain mass range are included in the analysis, otherwise one must resort to halo selections based on an observable that is not sensitive to halo bias variations [75].

The second method is to combine the large-scale measurements of galaxy-galaxy lensing and galaxy clustering, which yields the linear theory constraints on $\sigma_8\Omega_m^{0.55-1}$ [25, 27, 76]. In the formulation used here the method has very few theoretical assumptions, since it is based on large scale clustering and lensing, where the two probes trace the same LSS with the cross-correlation coefficient close to unity [27]. While the measurement uncertainties depend on mass via its volume and total abundance, this method works well for a broad range of mass, with the best constraints in SDSS corresponding to the range between the L_* galaxies to the low mass clusters, which allows multiple galaxy samples to be combined to statistically tighten the resulting constraints. Furthermore, this method can be greatly improved with larger number density of background source galaxies at higher redshift in the future surveys, as its measurement uncertainties lag behind the clustering measurement uncertainties in the SDSS. In contrast, the cosmological constraint is the combination of $\sigma_8\Omega_m$, such that other constraints should be combined to break the degeneracy. The future galaxy surveys we considered improve the constraints derived for the SDSS, mainly by going deeper in redshift and covering larger sky. However, the photometric galaxy surveys like the DES lack capability to map galaxies in three-dimensional positions and measure the angular clustering measurements, which become the limiting factor given the substantial improvements in lensing measurements.

The third method is to utilize the (galaxy or cluster) abundance information, in conjunction with the lensing measurements of mean masses of galaxy samples. Due to the exponential sensitivity of the halo mass function to cosmological parameters in the clusters range, this method can yield some of the best constraints among the three methods, and the mass range of the LRGs to low mass clusters works best for this method too. The constraints are, however, comparable to the combined method I+II, which use both large-scale and small-scale lensing information, in addition to the large-scale clustering information. While the abundance is modeled by assuming a log-normal scatter in the mass-observable relation, our investigation of the systematic errors in this method shows that the systematic errors such as the presence α_g of invisible halos and the skewness S_3 of the probability distribution in the mass-observable relation are relatively innocuous given the present level of uncertainties in those parameters. For the future surveys this method continues to yield competitive constraints, but is not superior to the combined method I+II. The methods I and II do not use abundance information and are thus not sensitive to the systematics associated with that, such as identifying multiple clusters in the same halo.

We also compared the derived constraints to those from cosmic shear measurements that use shear-shear correlations. These can use information to significantly smaller scales and as a result can provide tighter constraints, despite the two-dimensional analysis assumed here. However, we argue that some of the gains cannot be achieved because of the baryonic effects [84], and more importantly, the sample variance and the nonlinear evolution of the matter trispectrum make the lensing power spectra on small scales highly correlated [80–82], setting the lower limit to the figure of merit one can obtain from the lensing power spectrum. Consequently, the constraints from the cosmic shear measurements are as strong as that from the combined method I+II. Furthermore, shear-shear analysis may also be more sensitive to the various spurious systematics such as variable PSF. Considering the serious systematic uncertainties present in the cosmic shear method it is useful to consider alternative methods, and the three methods explored in this paper are the best alternatives proposed so far in measuring perturbations of dark matter, apart from redshift-space distortions which we do not consider in this paper. Their combined power is comparable to that of the shear-shear power spectrum, with very different systematics errors. In particular, the combined lensing and clustering analysis method, which combines the methods I and II of this paper, is a method that has not been discussed much in the literature, yet it gives predicted errors for SDSS that are comparable to the better known cluster abundance method with weak lensing calibration (method III). The method is currently being applied to the SDSS data and we expect this method will play an important role in the future surveys as well.

Acknowledgments

We acknowledge useful discussions with Pat McDonald and Rachel Mandelbaum. We thank Chris Hirata for providing us with trispectrum contribution to the cosmic shear measurements. This work is supported by the Swiss National Foundation (SNF) under contract 200021-116696/1 and WCU grant R32-10130. J.Y. is supported by the SNF Ambizione Grant.

[1] D. G. York et al., Astron. J. **120**, 1579 (2000), arXiv:astro-ph/0006396.

[2] K. N. Abazajian et al., Astrophys. J. Suppl. Ser. **182**, 543 (2009), arXiv:0812.0649.

[3] N. Kaiser, Astrophys. J. Lett. **284**, L9 (1984).
[4] N. Kaiser, Mon. Not. R. Astron. Soc. **227**, 1 (1987).
[5] M. Tegmark et al., Phys. Rev. D **69**, 103501 (2004), arXiv:astro-ph/0310723.
[6] U. Seljak, Mon. Not. R. Astron. Soc. **325**, 1359 (2001), astro-ph/0009016.
[7] M. White, Mon. Not. R. Astron. Soc. **321**, 1 (2001), arXiv:astro-ph/0005085.
[8] J. L. Tinker, D. H. Weinberg, and Z. Zheng, Mon. Not. R. Astron. Soc. **368**, 85 (2006), astro-ph/0501029.
[9] U. Seljak and P. McDonald, J. Cosmol. Astropart. Phys. **11**, 39 (2011), arXiv:1109.1888.
[10] B. A. Reid and M. White, Mon. Not. R. Astron. Soc. **417**, 1913 (2011), arXiv:1105.4165.
[11] Y. Mellier, Annu. Rev. Astron. Astrophys. **37**, 127 (1999), arXiv:9812172.
[12] M. Bartelmann and P. Schneider, Phys. Rep. **340**, 291 (2001), arXiv:9912508.
[13] A. Refregier, Annu. Rev. Astron. Astrophys. **41**, 645 (2003), arXiv:0307212.
[14] J. A. Tyson, F. Valdes, J. F. Jarvis, and A. P. Mills, Jr., Astrophys. J. Lett. **281**, L59 (1984).
[15] T. G. Brainerd, R. D. Blandford, and I. Smail, Astrophys. J. **466**, 623 (1996), astro-ph/9503073.
[16] P. Fischer and et al., Astron. J. **120**, 1198 (2000), astro-ph/9912119.
[17] E. S. Sheldon et al., Astron. J. **127**, 2544 (2004), astro-ph/0312036.
[18] R. Mandelbaum, U. Seljak, G. Kauffmann, C. M. Hirata, and J. Brinkmann, Mon. Not. R. Astron. Soc. **368**, 715 (2006), astro-ph/0511164.
[19] R. Mandelbaum, U. Seljak, R. J. Cool, M. Blanton, C. M. Hirata, and J. Brinkmann, Mon. Not. R. Astron. Soc. **372**, 758 (2006), astro-ph/0605476.
[20] R. Mandelbaum, U. Seljak, T. Baldauf, and R. E. Smith, Mon. Not. R. Astron. Soc. **405**, 2078 (2010), arXiv:0911.4972.
[21] J. Miralda-Escudé, Astrophys. J. **370**, 1 (1991).
[22] J. Guzik and U. Seljak, Mon. Not. R. Astron. Soc. **335**, 311 (2002), astro-ph/0201448.
[23] W. Hu and B. Jain, Phys. Rev. D **70**, 043009 (2004), arXiv:0312395.
[24] R. Mandelbaum, A. Tasitsiomi, U. Seljak, A. V. Kravtsov, and R. H. Wechsler, Mon. Not. R. Astron. Soc. **362**, 1451 (2005), astro-ph/0410711.
[25] J. Yoo, J. L. Tinker, D. H. Weinberg, Z. Zheng, N. Katz, and R. Davé, Astrophys. J. **652**, 26 (2006), astro-ph/0511580.
[26] M. Cacciato, F. C. van den Bosch, S. More, R. Li, H. J. Mo, and X. Yang, Mon. Not. R. Astron. Soc. **394**, 929 (2009), 0807.4932.
[27] T. Baldauf, R. E. Smith, U. Seljak, and R. Mandelbaum, Phys. Rev. D **81**, 063531 (2010), 0911.4973.
[28] A. Leauthaud, J. Tinker, P. S. Behroozi, M. T. Busha, and R. H. Wechsler, Astrophys. J. **738**, 45 (2011), arXiv:1103.2077.
[29] M. Cacciato, F. C. van den Bosch, S. More, H. Mo, and X. Yang, ArXiv e-prints (2012), 1207.0503.
[30] I. Zehavi and et al., Astrophys. J. **736**, 59 (2011), arXiv:1005.2413.
[31] R. Mandelbaum, U. Seljak, and C. M. Hirata, J. Cosmol. Astropart. Phys. **8**, 6 (2008), arXiv:0805.2552.
[32] U. Seljak, Mon. Not. R. Astron. Soc. **318**, 203 (2000), astro-ph/0001493.
[33] C.-P. Ma and J. N. Fry, Astrophys. J. **543**, 503 (2000), astro-ph/0003343.
[34] J. A. Peacock and R. E. Smith, Mon. Not. R. Astron. Soc. **318**, 1144 (2000), astro-ph/0005010.
[35] R. Scoccimarro, R. K. Sheth, L. Hui, and B. Jain, Astrophys. J. **546**, 20 (2001), astro-ph/0006319.
[36] A. A. Berlind and D. H. Weinberg, Astrophys. J. **575**, 587 (2002), astro-ph/0109001.
[37] A. Cooray and R. Sheth, Phys. Rep. **372**, 1 (2002), astro-ph/0206508.
[38] U. Seljak and et al., Phys. Rev. D **71**, 103515 (2005), astro-ph/0407372.
[39] W. Hu, Phys. Rev. D **67**, 081304 (2003), arXiv:0301416.
[40] M. Lima and W. Hu, Phys. Rev. D **70**, 043504 (2004), arXiv:astro-ph/0401559.
[41] R. Mandelbaum and U. Seljak, J. Cosmol. Astropart. Phys. **6**, 24 (2007), arXiv:astro-ph/0703114.
[42] R. D. Blandford, A. B. Saust, T. G. Brainerd, and J. V. Villumsen, Mon. Not. R. Astron. Soc. **251**, 600 (1991).
[43] J. Miralda-Escudé, Astrophys. J. **380**, 1 (1991).
[44] N. Kaiser, Astrophys. J. **388**, 272 (1992).
[45] C. M. Hirata, R. Mandelbaum, U. Seljak, J. Guzik, N. Padmanabhan, C. Blake, J. Brinkmann, T. Budávari, A. Connolly, I. Csabai, et al., Mon. Not. R. Astron. Soc. **353**, 529 (2004), arXiv:0403255.
[46] R. Mandelbaum, C. M. Hirata, U. Seljak, J. Guzik, N. Padmanabhan, C. Blake, M. R. Blanton, R. Lupton, and J. Brinkmann, Mon. Not. R. Astron. Soc. **361**, 1287 (2005), astro-ph/0501201.
[47] D. Huterer, M. Takada, G. Bernstein, and B. Jain, Mon. Not. R. Astron. Soc. **366**, 101 (2006), arXiv:0506030.
[48] J. Blazek, M. McQuinn, and U. Seljak, J. Cosmol. Astropart. Phys. **5**, 10 (2011), 1101.4017.
[49] R. Nakajima, R. Mandelbaum, U. Seljak, J. D. Cohn, R. Reyes, and R. Cool, Mon. Not. R. Astron. Soc. **420**, 3240 (2012), 1107.1395.
[50] D. J. Bacon, A. R. Refregier, and R. S. Ellis, Mon. Not. R. Astron. Soc. **318**, 625 (2000), arXiv:0003008.
[51] N. Kaiser, G. Wilson, and G. A. Luppino, ArXiv Astrophysics e-prints (2000), arXiv:0003338.
[52] D. M. Wittman, J. A. Tyson, D. Kirkman, I. Dell'Antonio, and G. Bernstein, Nature (London) **405**, 143 (2000), arXiv:0003014.
[53] L. Van Waerbeke, Y. Mellier, T. Erben, J. C. Cuillandre, F. Bernardeau, R. Maoli, E. Bertin, H. J. McCracken, O. Le Fèvre, B. Fort, et al., Astron. Astrophys. **358**, 30 (2000), arXiv:0002500.
[54] C. Heymans, M. L. Brown, M. Barden, J. A. R. Caldwell, K. Jahnke, C. Y. Peng, H.-W. Rix, A. Taylor, S. V. W. Beckwith, E. F. Bell, et al., Mon. Not. R. Astron. Soc. **361**, 160 (2005), arXiv:0411324.
[55] A. Leauthaud, R. Massey, J.-P. Kneib, J. Rhodes, D. E. Johnston, P. Capak, C. Heymans, R. S. Ellis, A. M. Koekemoer, O. Le Fèvre, et al., Astrophys. J. Suppl. Ser. **172**, 219 (2007), arXiv:0702359.
[56] H. Hoekstra, Y. Mellier, L. van Waerbeke, E. Semboloni, L. Fu, M. J. Hudson, L. C. Parker, I. Tereno, and K. Benabed, Astrophys. J. **647**, 116 (2006), arXiv:0511089.
[57] E. M. Huff, C. M. Hirata, R. Mandelbaum, D. Schlegel, U. Seljak, and R. H. Lupton (2011), arXiv:1111.6958.
[58] E. M. Huff, T. Eifler, C. M. Hirata, R. Mandelbaum, D. Schlegel, and U. Seljak (2011), arXiv:1112.3143.
[59] H. Lin, S. Dodelson, H.-J. Seo, M. Soares-Santos, J. Annis, J. Hao, D. Johnston, J. M. Kubo, R. R. R. Reis, and M. Simet, ArXiv e-prints (2011), arXiv:1111.6622.
[60] T. Okumura, U. Seljak, and V. Desjacques, ArXiv e-prints (2012), 1206.4070.
[61] I. Zehavi and et al., Astrophys. J. **621**, 22 (2005), astro-

ph/0411557.
[62] D. J. Eisenstein, M. Blanton, I. Zehavi, N. Bahcall, J. Brinkmann, J. Loveday, A. Meiksin, and D. Schneider, Astrophys. J. **619**, 178 (2005), arXiv:astro-ph/0411559.
[63] R. J. Cool, D. J. Eisenstein, X. Fan, M. Fukugita, L. Jiang, C. Maraston, A. Meiksin, D. P. Schneider, and D. A. Wake, Astrophys. J. **682**, 919 (2008), 0804.4516.
[64] B. P. Koester et al., Astrophys. J. **660**, 239 (2007), arXiv:astro-ph/0701265.
[65] E. Rozo, R. H. Wechsler, E. S. Rykoff, J. T. Annis, M. R. Becker, A. E. Evrard, J. A. Frieman, S. M. Hansen, J. Hao, D. E. Johnston, et al., Astrophys. J. **708**, 645 (2010), arXiv:0902.3702.
[66] Z. Zheng, I. Zehavi, D. J. Eisenstein, D. H. Weinberg, and Y. P. Jing, Astrophys. J. **707**, 554 (2009), arXiv:0809.1868.
[67] B. A. Reid and D. N. Spergel, Astrophys. J. **698**, 143 (2009), arXiv:0809.4505.
[68] M. R. Blanton, H. Lin, R. H. Lupton, F. M. Maley, N. Young, I. Zehavi, and J. Loveday, Astron. J. **125**, 2276 (2003), arXiv:0105535.
[69] J. Tinker, A. V. Kravtsov, A. Klypin, K. Abazajian, M. Warren, G. Yepes, S. Gottlöber, and D. E. Holz, Astrophys. J. **688**, 709 (2008), 0803.2706.
[70] J. L. Tinker, B. E. Robertson, A. V. Kravtsov, A. Klypin, M. S. Warren, G. Yepes, and S. Gottlöber, Astrophys. J. **724**, 878 (2010), arXiv:1001.3162.
[71] J. F. Navarro, C. S. Frenk, and S. D. M. White, Astrophys. J. **490**, 493 (1997), astro-ph/9611107.
[72] C. O. Wright and T. G. Brainerd, Astrophys. J. **534**, 34 (2000).
[73] L. Gao, V. Springel, and S. D. M. White, Mon. Not. R. Astron. Soc. **363**, L66 (2005), astro-ph/0506510.
[74] R. H. Wechsler, A. R. Zentner, J. S. Bullock, A. V. Kravtsov, and B. Allgood, Astrophys. J. **652**, 71 (2006), arXiv:astro-ph/0512416.
[75] D. J. Croton, L. Gao, and S. D. M. White, Mon. Not. R. Astron. Soc. **374**, 1303 (2007), arXiv:astro-ph/0605636.
[76] R. Mandelbaum, A. Slosar, T. Baldauf, U. Seljak, C. M. Hirata, R. Nakajima, R. Reyes, and R. E. Smith, ArXiv e-prints (2012), 1207.1120.
[77] B. Jain and U. Seljak, Astrophys. J. **484**, 560 (1997), arXiv:astro-ph/9611077.
[78] W. Hu and A. V. Kravtsov, Astrophys. J. **584**, 702 (2003), arXiv:0203169.
[79] T. Matsubara, Astrophys. J. **525**, 543 (1999), arXiv:9906029.
[80] A. Cooray and W. Hu, Astrophys. J. **554**, 56 (2001), arXiv:astro-ph/0012087.
[81] A. Albrecht, L. Amendola, G. Bernstein, D. Clowe, D. Eisenstein, L. Guzzo, C. Hirata, D. Huterer, R. Kirshner, E. Kolb, et al., ArXiv e-prints (2009), 0901.0721.
[82] M. Sato, T. Hamana, R. Takahashi, M. Takada, N. Yoshida, T. Matsubara, and N. Sugiyama, Astrophys. J. **701**, 945 (2009), 0906.2237.
[83] Z. Ma, W. Hu, and D. Huterer, Astrophys. J. **636**, 21 (2006), arXiv:0506614.
[84] E. Semboloni, H. Hoekstra, J. Schaye, M. P. van Daalen, and I. G. McCarthy, Mon. Not. R. Astron. Soc. **417**, 2020 (2011), 1105.1075.
[85] D. H. Weinberg, M. J. Mortonson, D. J. Eisenstein, C. Hirata, A. G. Riess, and E. Rozo, ArXiv e-prints (2012), arXiv:1201.2434.
[86] E. Rozo, E. S. Rykoff, A. Evrard, M. Becker, T. McKay, R. H. Wechsler, B. P. Koester, J. Hao, S. Hansen, E. Sheldon, et al., Astrophys. J. **699**, 768 (2009), 0809.2794.
[87] M. Oguri and M. Takada, Phys. Rev. D **83**, 023008 (2011), 1010.0744.
[88] H. J. Mo and S. D. M. White, Mon. Not. R. Astron. Soc. **282**, 347 (1996), arXiv:9512127.
[89] R. K. Sheth and G. Tormen, Mon. Not. R. Astron. Soc. **308**, 119 (1999), astro-ph/9901122.
[90] R. K. Sheth, H. J. Mo, and G. Tormen, Mon. Not. R. Astron. Soc. **323**, 1 (2001), astro-ph/9907024.
[91] U. Seljak and M. S. Warren, Mon. Not. R. Astron. Soc. **355**, 129 (2004), astro-ph/0403698.